

UCSF

UC San Francisco Electronic Theses and Dissertations

Title

Investigation of amyloid polymorphism and its role in Alzheimer's disease pathogenesis

Permalink

<https://escholarship.org/uc/item/0p0577hg>

Author

Maxwell, Alison

Publication Date

2021

Peer reviewed|Thesis/dissertation

Investigation of amyloid polymorphism and its role in Alzheimer's disease pathogenesis

by
Alison Maxwell

DISSERTATION

Submitted in partial satisfaction of the requirements for degree of
DOCTOR OF PHILOSOPHY

in

Chemistry and Chemical Biology

in the

GRADUATE DIVISION

of the

UNIVERSITY OF CALIFORNIA, SAN FRANCISCO

Approved:

DocuSigned by:

William Degrado

582727E949C7441...

William Degrado

Chair

DocuSigned by:

CARLO CONDELLO

DocuSigned by:

Jason E. Gestwicki

DocuSigned by:

Lea Grinberg

DocuSigned by:

Daniel Southworth

031AA0767EFF409...

CARLO CONDELLO

Jason E. Gestwicki

Lea Grinberg

Daniel Southworth

Committee Members

Copyright 2021

by

Alison Maxwell

To Wilder, for your enduring support.

ACKNOWLEDGMENTS

The process of earning my PhD has challenged me in many ways I expected and many more that I did not. With every setback, there has been a dozen people to pick me up and keep me moving forward. More people than I can possibly acknowledge have enabled this accomplishment, but here is a start.

Wilder, to whom this dissertation is dedicated: you are the smartest, yet most humble and kind, person I know. You know better than anyone how much I struggled, and how much I relied on you to get me through. Thank you for your endless patience, love, and support.

My family has been the foundation of all that I have accomplished. From encouraging every academic and extracurricular activity I sought out in high school, to enabling a college experience that allowed me to flourish, to valuing my career goals and life as an adult—my parents have done everything to set me up for success. Thank you for continuing to be interested and supportive of everything I do. To my brother, Stephen: thank you for always being one step ahead, testing the path and keeping me grounded. Your judgement-free enthusiasm for all my endeavors has been more healing than you know. And Kelly and Erin, my sisters at heart, the constancy of your friendship and love has sustained me through every challenge.

Thank you to all of my teammates on West Valley Track Club, especially Katie, Karen, Amy, and Emma. Being among such strong, tenacious, and compassionate women has been an invigorating experience and welcome distraction. I didn't know how fortunate I would be to find this community, and how much I would need it to keep me sane.

I owe thanks to many colleagues and friends and UCSF for making this work come to life. I am lucky to have learned to navigate a PhD with Taia, Doug, and the entire 2016 CCB cohort; I

can't wait to see the incredible things they accomplish in science and beyond. Throughout my tenure in the DeGrado lab, Robert Newberry has consistently been a thoughtful, patient, and enthusiastic mentor; without him I wouldn't have believed I could finish this project or that it would have much worth. I am also grateful to Jack Nicoludis, Greg Merz, Sam Mann, Huong Kratochvil, Haifan Wu, Nick Polizzi, Sophia Tan, Hyunil Jo, and Bruk Mensa for their expert technical guidance; without them my research would have been largely ineffective. I am grateful to Drs. Sy Redding, Tanja Kortemme, Elizabeth Head, Frances Wiseman, and William Mobley for their encouragement and thoughtful advice; without them, I may not have had the motivation to finish this PhD. Thank you to Carlo Condello, who adopted me into his research group and donated so much of his time to my project; without him, I wouldn't have had a thesis project at all. And I am thankful to Madhy Garcia, Brianna Rivera, Weizhou Yue, Bailin Ye, and Abby Oehler for their scientific rigor and the many hours of time they dedicated to my experiments; without them I would have had far less data.

I am also indebted to the many people who molded me into a capable scientist. At Port Angeles High School, Keith Johnson and John Gallagher fostered both my academic rigor and my love of learning. Thank you to Dr. Peter Shultz for taking me on as a summer intern, and to Dr. Lubica Supekova for being a brilliant, patient, and enlightening mentor. At Middlebury College, I had the fortune to work with and learn from Dr. Molly Costanza-Robinson, whom I owe for my confidence in taking on impossible projects. And of course, I am immeasurably grateful to Dr. Roger Sandwick, my biggest cheerleader.

Most importantly, thank you to everyone who has donated or will donate their bodies to science. Without them, this work and so much more would not have been possible. The tissue samples used in Chapter 2 were supplied by the NIH NeuroBioBank; the August Pi i Sunyer

Biomedical Research Institute (IDIBAPS) Biobank (Barcelona, Spain); the University of California Alzheimer's Disease Research Center (UCI-ADRC, Irvine, CA), which is funded by NIH/NIA Grant P30AG066519; the UCSF Neurodegenerative Disease Brain Bank and Prof. William W. Seeley (UCSF Memory and Aging Center, San Francisco, CA); the University of Washington Neuropathology Core (Seattle, WA), which is supported by the Alzheimer's Disease Research Center (AG005136), the Adult Changes in Thought Study (AG006781), and the Morris K. Udall Center of Excellence for Parkinson's Disease Research (NS062684); the London Neurodegenerative Diseases Brain Bank (King's College London, England), which receives funding from the Medical Research Council UK and through the Brains for Dementia Research Project (jointly funded by the Alzheimer's Society and Alzheimer's Research UK); the Oxford Brain Bank, supported by the Medical Research Council (MRC), Brains for Dementia Research (BDR) (Alzheimer Society and Alzheimer Research UK), Autistica UK and the NIHR Oxford Biomedical Research Centre; the Langone Health Alzheimer's Disease Center (New York University, NY), which is supported by funding from NIH grant to the NYU Alzheimer's Disease Research Center, P30AG066512; and The Manchester Brain Bank (University of Manchester, England), which is part of the Brains for Dementia Research program, jointly funded by Alzheimer's Research UK and Alzheimer's Society.

This material is based on work supported by the National Science Foundation Graduate Research Fellowship Program under Grant No. 2034836 and by the NIH under Grants Nos. T32 GM064337 (A.M.M), RF1AG061874 (C.C. and W.F.D.) and P01AG002132 (C.C. and W.F.D.). Any opinions, findings, conclusions or recommendations expressed in this material are those of the author(s) and do not necessarily reflect the views of the NSF or NIH.

CONTRIBUTIONS

Chapter 1 represents unpublished work. All biochemical assays, confocal microscopy, electron microscopy, amyloid fibrillation, and peptide synthesis was conducted by Alison Maxwell. David Jacobson (University of Colorado, Boulder) did the atomic force microscopy experiments. Hyunil Jo and Haifan Wu provided invaluable guidance and assistance in peptide synthesis, purification, and characterization. Project oversight was provided by Carlo Condello and William DeGrado.

Chapter 2 is adapted from a manuscript that has been posted as a preprint on bioRxiv (doi:10.1101/2021.07.30.454527) and has been submitted for publication. Alison Maxwell designed the experiments; performed biochemical, histological, and microscopy-based experiments; conducted data analysis and management; and wrote the manuscript. Peng Yuan developed software to analyze the confocal micrographs. Brianna Rivera conducted biochemical experiments. Wilder Schaaf conducted computational analyses. Mihovil Mladinov provided advice on neuropathological analysis. Vee Prasher and Andrew Robinson provided brain tissue samples. William DeGrado oversaw the management of the project. Carlo Condello designed methodology, helped manage the project, and helped prepare the manuscript for publication.

ABSTRACT

Investigation of amyloid polymorphism and its role in Alzheimer's disease pathogenesis

Alison Maxwell

Amyloid fibrils are insoluble protein aggregates with a broad range of biophysical properties and biological functions. Potentially all proteins can form amyloids, each of which can adopt a multitude of distinct molecular conformations, or polymorphs. Characterizing the molecular structure of various polymorphs and linking these features to their function or pathology is a prevalent challenge across biology, medicine, and technology. In this dissertation, I explore multiple aspects of amyloid structure and its relationship to biology. In Chapter 1, I work towards expanding a fluorogenic dye toolkit that can report on structural differences among amyloids; determining the structural composition of fibrils generated from multiple distinct species of amyloid beta ($A\beta$); and interrogating the atomic connections governing a functional amyloid's macrostructure. In Chapter 2, I investigate the prevalence of different species of $A\beta$ along the trajectory of Alzheimer's disease (AD) pathology in Down syndrome (DS). In the latter work, I find that different subsets of $A\beta$ may predominate in the brain tissue of people with early compared to advanced AD pathology and that a more heterogeneous population of $A\beta$ species are present at the late stages of disease in DS.

TABLE OF CONTENTS

Chapter 1: Probing biophysical properties of amyloids using conformation-sensitive dyes and atomic force microscopy 1

1.1 Introduction 1

1.2 Methods 5

1.3 Results & Discussion. 9

1.4 References 21

Chapter 2: Emergence of distinct and heterogeneous strains of amyloid beta with advanced Alzheimer’s disease pathology in Down syndrome 24

2.1 Introduction 25

2.2 Methods 28

2.3 Results 34

2.4 Discussion 43

2.5 References 49

Appendix A: Supplementary information for Chapter 1 62

Appendix B: Supplementary information for Chapter 2 66

B.1 Methods 66

B.2 Results & Discussion 69

B.3 Additional Table and Figures 74

B.4 References 77

Appendix C: Individual case characteristics 78

Appendix D: IRB certification 87

LIST OF FIGURES

Figure 1.1: Preparation of A β fibril strains	6
Figure 1.2: BF-188 spectra allow for A β strain discrimination by PCA	10
Figure 1.3: FLIM discriminates between fibrils composed of different ratios of A β 40 and A β 42	14
Figure 1.4: Product characterization of catalytic amyloid peptide derivatization with sulfo DBCO-maleimide	16
Figure 1.5: Example images from initial AFM imaging experiments	17
Figure 2.1: A range of case ages, genotypes, and sexes comprise the study cohorts	34
Figure 2.2: Characterization of neuropathology using custom histological scoring and biochemistry	36
Figure 2.3: PCA performed on plaque-derived fluorescence spectra reveals a subset of conformational space unique to DS	40
Figure 2.4: Per-patient strain heterogeneity increases with advancing pathology	42
Figure B.1: Preliminary A β and tau prion-like activities in a cellular bioassay	72
Figure B.2: A β and tau scores relative to patient age at death	74
Figure B.3: Total protein and tau species concentrations in greater granularity	75
Figure B.4: Wavelength contributions to the principle component space	76
Figure B.5: Per-patient RMSD distributions by age, sex, and APOE	76

LIST OF TABLES

Table 2.1: A β and tau scoring criteria by pathological feature density	30
Table A.1: Spectral properties of dyes tested for conformation sensitivity	62
Table A.2: Spectral changes of BF-188/PBB5-stained A β fibrils compared to procedural elements	63
Table B.1: Primers and conditions used in APP copy number assay	68
Table B.2: APP copy number analysis of five DS subjects	70
Table B.3: <i>APOE</i> primers and conditions used in PCR and sequencing	74
Table C.1: Biological data and experimental inclusion of each case	78

LIST OF ABBREVIATIONS

A β	amyloid beta
AD	Alzheimer's disease
AD-DS	AD in Down syndrome
ADNC	AD neuropathological change
AFM	atomic force microscopy
ApoE	apolipoprotein E
APP	amyloid precursor protein
BH	brain homogenate
Chr21	chromosome 21
CN	copy number
cryo-EM	cryogenic EM
DS	Down syndrome
ΔC_T	difference in threshold cycle number
ΔR_n	difference in normalized reporter value
ELISA	enzyme-linked immunosorbent assay
EM	electron microscopy
fAD	familial AD
FLIM	fluorescence lifetime imaging microscopy
FRET	Förster (or fluorescence) resonance energy transfer
HTRF	homologous time-resolved fluorescence
IHC	immunohistochemistry

KDE	kernel density estimation
MANOVA	multivariate analysis of variance
NFT	neurofibrillary tangle
PCA	principal component analysis
PMI	post-mortem interval
PT21	partial trisomy of Chr21
pTau	phosphorylated tau
RMSD	root-mean-square deviation
sAD	sporadic AD
ssNMR	solid-state nuclear magnetic resonance
TEM	transmission EM
ThT	thioflavin T

CHAPTER 1

Probing biophysical properties of amyloid fibrils using conformation-sensitive dyes and atomic force microscopy

ABSTRACT

Interest in understanding the conformational landscape of amyloid fibrils spans biology, technology, and medicine. In contrast to high-resolution structural determination techniques, conformation-sensitive fluorescent probes enable sensitive yet high-throughput analysis of amyloid structural differences in a variety of sample types. In this work, we attempt to better understand amyloid fibrils by: (1) improving the discriminatory power of a fluorogenic amyloid dye toolkit, (2) determining the structural composition of fibrils generated from multiple distinct species of amyloid beta, and (3) probing the unfolding trajectory of a catalytic amyloid fibril using atomic force microscopy. While this work is unfinished and unpublished, it sets the stage for a more holistic understanding of amyloids and their structure.

1.1 INTRODUCTION

Amyloid fibrils are insoluble protein aggregates with immense stability and structural complexity, conferring them with a broad range of biophysical properties and biological functions. Many, perhaps all, soluble proteins are able to form amyloids regardless of their native structure. Functional amyloids support normal biological activity including adhesion and biofilm formation

in bacteria¹, spore development in fungi², rubber biosynthesis in plants³, and melanin synthesis in humans⁴. Many amyloids are also implicated in disease, such as prion protein (PrP) in spongiform encephalopathies⁵, islet amyloid polypeptide (IAPP) in Type II diabetes⁶, α -synuclein in Parkinson's disease⁷, and amyloid beta ($A\beta$) in Alzheimer's disease⁸. Furthermore, amyloids are emerging as useful tools in biotechnology, while their energetic favorability and stability implicate amyloids in the origin of life.

This biological diversity can be understood through the fibril formation pathway. Fibrillogenesis is initiated when a natively folded protein becomes destabilized, resulting in the formation of an aggregation-prone intermediate state⁹. Under certain conditions, the unfolded intermediates can overcome a kinetic barrier to form oligomers or protofibrils that serve as a nucleus for fibril formation¹⁰. These nuclei can then template the polymerization of hundreds of thousands of additional peptide monomers¹¹, resulting in fibrils that can be multiple micrometers in length. The resulting fibrils always have a cross- β -sheet structure¹², wherein continuous β -sheet strands run perpendicular to the fibril axis. These assemblies can be parallel or anti-parallel in orientation¹³, are dependent on specific interactions of side-chains¹⁴, and can have various twisted multi-filament ultrastructures¹⁵.

Different local minima in the folding energy landscape, influenced by environmental factors, can lead to a multitude of possible fibril structures for a single peptide, called polymorphs¹⁶. Packing, segmental, side-chain, and supramolecular assembly polymorphism all contribute to how amyloids interact with their environment and consequently how they may lead to various functional or pathological outcomes¹⁷. For example, the difference of an exposed charged-side chain would drastically change the surface charge distribution of a fibril and affect its ability to interact with other macromolecules. Different polymorph stabilities also impact fibril

length and shearing, which in turn would alter the rate of nucleation and further fibril formation¹⁸.

Considering the relevance of amyloids across biology, technology, and human health, many fields of research have interest in detecting various polymorphs and characterizing their structure. Doing so, however, is not trivial. Because fibril orderdness is one-dimensional, all but the shortest amyloid fragments are not amenable to three-dimensional crystallization¹⁷. Furthermore, the techniques that have been successful in determining amyloid structure (i.e., solid-state NMR (ssNMR) and electron microscopy (EM))¹⁹ are labor intensive, expensive, and require a soluble sample. The ability to more easily discern the type and level of different amyloid polymorphs in a sample of interest would provide critical insight into the functional roles of specific conformations, allowing more detailed structural efforts to focus on distinct, relevant strains.

Thus, there is a great need for a tool that can easily distinguish and classify different amyloids in high throughput. While fluorescent small-molecule probes like thioflavin-T (ThT) are commonly used to identify amyloid fibrils *in vivo* and *in vitro*, these dyes have historically been used only to signal the presence of amyloid rather than to distinguish between its conformational strains. Recently, Condello and colleagues showed that certain derivatives of common dyes can differentiate distinct A β strains in human brain samples.²⁰ The fluorescence of these dyes is highly sensitive to changes in local environment, such that any polymorphism may alter their emission spectra. Using this innovative concept, we sought to develop a method to clearly and efficiently identify distinct amyloid conformations by staining amyloids with optimized combinations of multiple fluorescent probes to define distinct multi-dimensional amyloid polymorph “fingerprints”. If successful, this method would allow for the rapid identification of structural differences among amyloids, enabling new insights into their structure-function relationships.

In this work, we aimed to answer the following questions: What combinations of dyes can together provide the most discriminating power? Can such a set distinguish among *all* strains of a given amyloid? We sought to transform our strain-sensitive dye method into a high-dimensional and multi-functional tool by combinatorially using dyes of different relative affinities, Förster resonance energy transfer (FRET) interactions, binding modes, and other physical properties. Because fluorescence differences reflect relative probe binding modes, combining dyes should enable unparalleled discrimination among different protein conformations.

Using confocal microscopy, we measured the spectral information of more than ten dyes bound to amyloid and deconvolved them by principle component analysis (PCA), projecting subtle changes into well-resolved 2D space. This enabled us to begin to define a distinct “fingerprint” for multiple species of A β . We also identified a promising FRET pair of the dyes BF-188 and PBB5, which had major differences in their relative intensities when bound to the various A β fibrils. With continued future optimization of this dye set, this work could be expanded to other amyloids such as α -synuclein or curli protein, enabling applications across technology and disease.

A second aim of this work was to determine whether we better understand the amyloid assembly pathway using atomic force microscopy (AFM). Though the fibril formation pathway is broadly understood, the multitude of fine structural transitions that occur to allow first for nucleation and then templating of the amyloid peptide have been difficult to characterize. In order to better understand the folding of individual peptide monomers into fibrils, we sought to test whether single amyloid peptides could be pulled from a fibril using AFM optimized for one-microsecond resolution. This technique has recently been utilized to reveal the complex dynamics of bacteriorhodopsin assembly by Yu and colleagues in the Perkins group²¹. Thus, through a collaboration with individuals in the same group, we probed the dynamics of a published *de novo*

designed functional amyloid that binds Zn^{2+} . This effort stagnated due to difficulty in reliably adhering fibrils to the AFM substrate, but the synthetic method we developed and conditions we optimized should facilitate future efforts.

1.2 METHODS

In vitro fibrillization of A β 40 and A β 42 mixtures

A β 40 and A β 42 fibrils were generated *in vitro* from commercial ultra-pure HFIP-prepared recombinant peptide (rPeptide cat #s A-1153-2 and A-1163-2) and from synthetic A β 40 (gift from Dr. Hyunil Jo). The lyophilized powder (1 mg) was dissolved in HFIP with 5 min of water bath sonication at room temperature to make 200 μ L of a 5 mg/mL solution. Each solution was aliquoted into five low-binding microcentrifuge tubes in varying volumes such that the tubes contained different ratios of A β 40:A β 42 as outlined in **Figure 1.1**. Two versions of the mixtures were prepared: recombinant A β 42 mixed with either recombinant or synthetic A β 40. The mixtures were briefly vortexed immediately after the addition of the second peptide solution. To evaporate the HFIP, tubes were air dried overnight, then vacuum evaporated for 30 min. The dry peptide films were then dissolved in 20 μ L ultra-high-grade DMSO with brief vortexing and 5 minutes of water bath sonication. The DMSO solution was diluted in 980 μ L NaPO₂H₄ buffer (pH 7.2) and pipetted gently to mix. Fibrillation was conducted at 37 °C with 900 rpm shaking for 72 hours. To remove DMSO and any remaining monomer, fibril solutions were ultracentrifuged at 48,000 $\times g$ for 1 h at 4 °C, aspirated, resuspended in 500 μ L buffer, and stored at 4 °C until use.

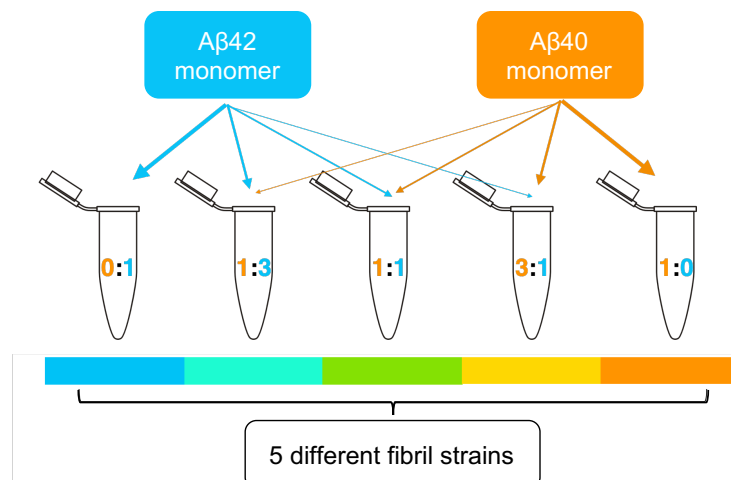


Figure 1.1. Preparation of A β fibril strains. A β 40 and A β 42 (40, 30, 20, and 10 μ L of 5 mg/mL monomer, as indicated by arrow linewidths) were mixed in different ratios and shaken at 900 rpm at 37 $^{\circ}$ C for 72 h. The resulting fibrils were purified and used in subsequent dye experiments.

Dye profiling using confocal microscopy

Master mixes of the 0.4 mg/mL A β fibril mixtures were prepared at 0.16 mg/mL in water and then diluted two-fold in warm 1% low melting-point agarose. Three 20- μ L replicates of each mixture were added to the wells of a 384-well, clear-bottomed plate. Dye solutions were prepared 1-50 μ M in water from 5 mM DMSO stocks for the dyes THK-265, THK-523, PBB5, Nile red, ThT, CRANAD-2, CRANAD-3, FSB, BAP-1, NIAD-4, BF-188, BSB, and Thiazole red. Fifty microliters of each dye solution were added to the wells and shaken at for 30 min at room temperature. Dyes were aspirated and the wells washed with water for 10 min, after which 50 μ L of fresh water was left in the wells to maintain gel hydration. For dye combination (putative FRET) experiments, stock solutions of the combined dyes (5 μ M each) were aliquoted and stored at -20 $^{\circ}$ C prior to staining.

For photobleaching tests, two free-radical scavengers 1,4-Diazoabicyclo[2.2.2]octane (DABCO, 50 mg/mL in water) or 6-hydroxy-2,5,7,8-tetramethylchroman-2-carbonsaure (Trolox, 10 μ M in water) were used in place of water to prepare the dye staining solutions. These solutions were not removed from the wells, nor were the wells washed, prior to imaging. Separately,

PermaFluor aqueous mounting medium (Thermo Fisher Scientific, EpreDia™ #TA006FM) was tested in place of 1% agarose during the initial fibril immobilization step.

Labelled fibril aggregates were imaged in the spectral (Lambda) scan mode of a Leica SP8 confocal microscope using a 63x water immersion lens (1.1 NA) and a HyD detector at 512- \times 512-pixel resolution. For each field-of-view, the optical plane was moved to the center of the z-stack volume for a given A β deposit. Dyes were excited with 405, 561, 594, and 633 nm lasers. For each laser that resulted in sufficient fluorescence intensity to be detected, emission was acquired from approximately the excitation wavelength to 780 nm in 9-nm steps using a sliding 15-nm-wide detection window.

Fluorescence lifetime imaging microscopy (FLIM)

Aggregates were suspended in agarose gel in a microplate as for spectral experiments. Dyes were tested both in the presence and absence of amyloid in order to determine lifetimes specific to the bound state. FLIM was carried out using a Leica Stellaris 8 Falcon FLIM-STED confocal microscope in Live Data Mode. Integrated analysis software was used to determine the number of exponentials appropriate for analysis.

Synthesis and fibrillization of Zn²⁺ catalytic amyloid peptide

To understand the dynamics of amyloid unfolding, we chemically synthesized a version of a Zn²⁺-mediated amyloid fibril that catalyzes ester hydrolysis²² with a glycine spacer and cysteine handle for derivatization. Ac-CGGGG-IHVHLQI-CONH₂ was synthesized on a 0.1-mmol scale using Fmoc solid-phase synthesis and was purified by reverse-phase HPLC to >98% purity. Peptide mass was verified by MALDI-TOF mass spectrometry. A portion of the peptide was

derivatized by mixing sulfo DBCO-maleimide ($C_{28}H_{26}N_4O_8S$, Click Chemistry Tools #1230) dissolved in water with equimolar peptide dissolved in HFIP in the presence of 0.1% N,N-diisopropylethylamine.

To make fibrils that could attach to a functionalized AFM tip, the labelled and parent peptide were mixed 1:10 and 1:50 in ultracentrifugation vials, dissolved in 10 mM HCl containing 8 M urea, and diluted 10-fold to 0.5 mg/mL in 25 mM Tris buffer (pH 8). The solutions were incubated at 30 min at room temperature with 900 rpm shaking. The fibrils were isolated with ultracentrifugation followed with a Tris buffer washing step to remove residual urea. Fibril formation was confirmed using a ThT assay (8 μ M ThT and 0.5 mg/mL fibrils) with 444/485 nm emission/excitation on a microplate fluorimeter.

Synthesis and fibrillization of R3 “tiny” tau

For AFM substrate adhesion troubleshooting experiments, a well-studied (in our hands) truncated isoform of tau was tested. VQIVYKPVDLSKVTSK-GGGGC was synthesized, derivatized, and purified as described for the Zn^{2+} catalytic amyloid peptide. Mass was verified by MALDI-TOF. Fibrils were formed of either 1:10 or 1:50 derivatized:parent peptide by shaking at 1000 rpm for 96 h at 37 °C. Fibril formation was verified by ThT.

Electron microscopy

Formation of A β fibril mixtures and catalytic amyloid was confirmed using transmission electron tomography (TEM). Sample aliquots were adsorbed onto 200-mesh copper grids for 2 min, sequentially washed twice in 0.1 M and twice in 0.01 M ammonium acetate, and then stained twice with 2% uranyl acetate. Uranyl acetate was always freshly prepared from powder and filtered

using a 0.2 μm syringe filter immediately before staining. An FEI Tecnai T12 electron microscope was used to obtain the micrographs.

Atomic force microscopy

All AFM was performed at the University of Colorado by Dr. David Jacobson based on a previously described method²¹. As a first test of detecting fibril features by AFM, fibrils of 1:10 parent to derivatized amyloid peptide were incubated overnight at 4 °C on an azide-functionalized substrate. Then, an attempt to pull on the amyloid was made by electrostatically adhering the fibrils to a charged mica surface and pulling using an azide-functionalized AFM tip. Multiple conditions were tested, with the most promising involving depositing the stock solution (200 $\mu\text{g}/\text{mL}$ of the 1:10 sample) on freshly cleaved mica, letting it stand for about a half hour, and then imaging in liquid without any rinsing.

1.3 RESULTS & DISCUSSION

Fluorogenic amyloid dyes can discriminate fibrils of mixed A β 40 and A β 42 monomer

We aimed to investigate which dyes or sets of dyes could discriminate fibrils comprised of different ratios of A β 40 and A β 42. We were further curious whether a fibril comprised of mixed species would adopt a conformation more similar to either unmixed parent peptide or have its own, unique conformation. Fibrils were prepared from lyophilized monomer under identical conditions. We confirmed fibril formation by ThT (data not shown) and TEM (**Figure 1.2A-C**), which showed heterogenous ultrastructure within a single preparation, including both fibril fragments and long, untwisted fibers. Considering that A β is notoriously sensitive to even subtle changes in

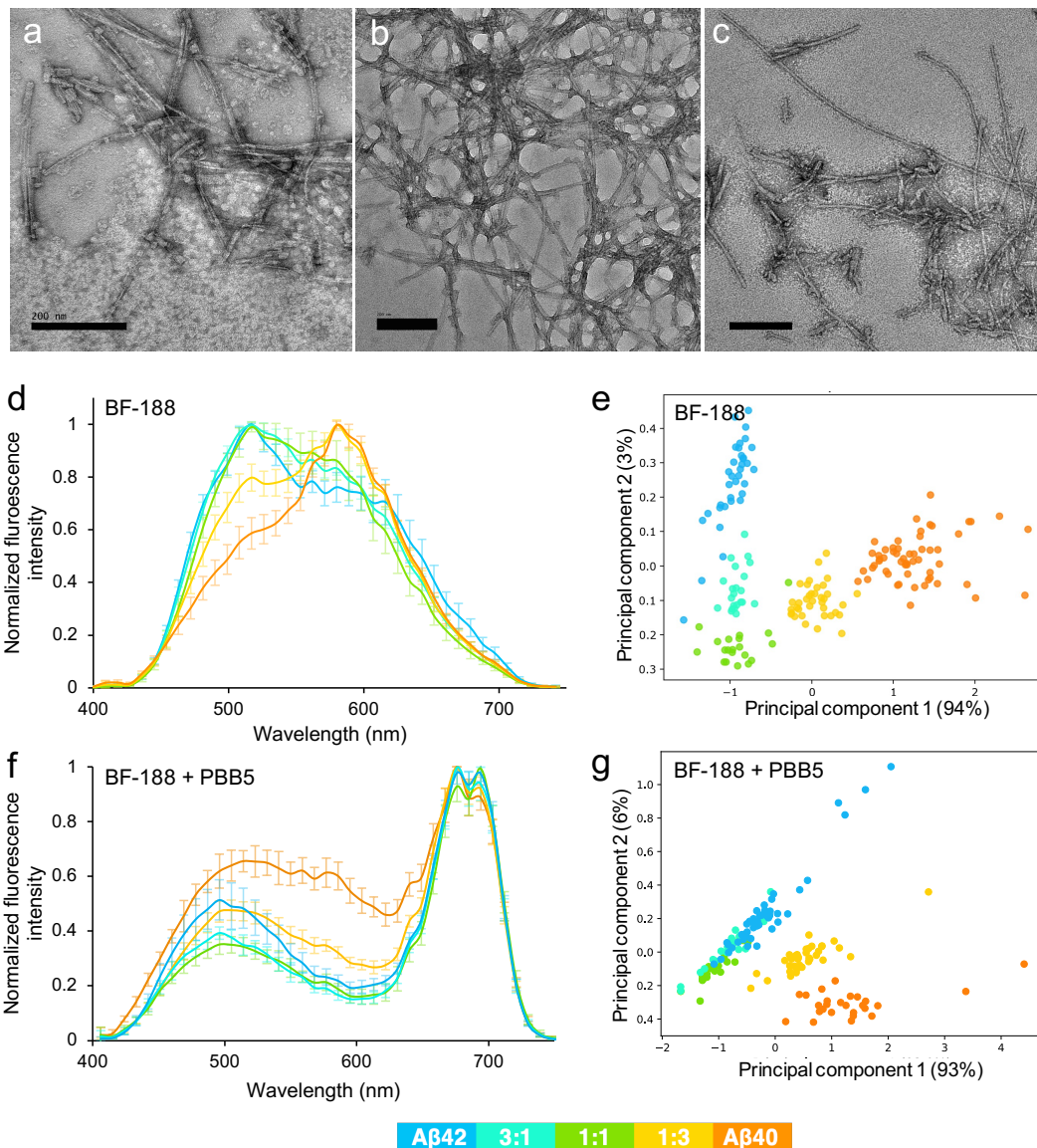


Figure 1.2. BF-188 spectra allow for A β strain discrimination by PCA. Fibrils formed of A β 40, A β 42, and mixtures of the two peptides were formed *in vitro*. (A-B) Formation of fibrils was confirmed by TEM, with examples of A β 40 fibrils from two different batch preparations shown. (C) Example of A β 42 fibrils formed shown. All scale bars = 200 nm. Aggregates of these fibrils were suspended in agarose gel in a microplate and stained with either (D-E) 5 μ M BF-188 dye or (F-G) a combination of 5 μ M BF-188 and 5 μ M PBB5. Amyloid-specific fluorescence was detected using confocal microscopy with 405 nm laser excitation. Spectra were normalized to the aggregate's peak intensity. The averages of 30-60 aggregates are shown +/- standard deviation. The fibril strains are clearly differentiated by BF-188 and are well separated by PCA. The addition of a second dye does not improve discrimination, likely in part due to the diminished differentiation of the BF-188 portion of the spectrum

fibrillization conditions, we made every effort to precisely replicate conditions across batches. TEM nonetheless reveals that there was possibly some variation in the final fibrils, as can be observed in the A β 40 fibrils from different batches shown in **Figure 1.2A-B**. However, the micrographs are likely not representative of the entire preparation, since deposition of fibrils on the EM grid was sparse. Therefore, while it may have been possible to compare subsequent experimental results across batches, we took caution to only compare within-batch data.

We stained fibril aggregates suspended in agarose gel in microplate wells with various fluorogenic amyloid dyes, some of which had been previously been tested in our hands but others which we identified as possible polymorph-sensitive candidates from the literature. We collected their fluorescence emission spectra with multiple laser excitation wavelengths using confocal microscopy. All dyes tested and their peak emission wavelength(s) are listed in **Table A.1**. Many dyes did not have significantly different emission spectra when bound to A β 40 versus A β 42 fibrils. The previously-confirmed conformation-sensitive dyes BF-188 (**Figure 1.2D**) and FSB clearly discriminated between all five fibril types. Using PCA to assess the separation showed nearly 100% separation between all fibril types (**Figure 1.2E**). Three other dyes showed promising discriminatory power: CRANAD-3, BAP-1, and THK-265 (**Table A.1**).

We further sought to identify a FRET donor-acceptor pair that would report on multiple probe binding sites with a single excitation step as well as report on the spatial relationship between the two (or more) sites. BF-188 was the clear choice for the donor, because it was by far the brightest dye and was conformationally sensitive. The best FRET acceptor, then, would also be conformationally sensitive (i.e. emit different spectra when bound to A β 40 and A β 42 fibrils) and would fluoresce brightly with 500-600 nm excitation, which is in the range of the peak emission wavelength(s) of BF-188. Though the above-mentioned dyes seemed promising in this regard,

they emitted only extremely dimly with 405 nm excitation of BF-188 (data not shown). We therefore next tried combining BF-188 with Nile red and, separately, with PBB5, two dyes that were not conformationally sensitive in initial tests but whose absorption spectra were well matched to the emission of BF-188. Nile red emission was far too dim (data not shown), possibly due to low FRET efficiency or reduced quantum yield.

PBB5, however, seemed to be a successful FRET acceptor, emitting brightly in the presence of BF-188 (**Figure 1.2F**). Most notably, the relative intensities of the two dyes appeared to be markedly different in fibrils comprised entirely of A β 40 compared to those of A β 42. However, when differentiated by PCA, the combined dyes did not yield better separation compared to using BF-188 alone (**Figure 1.2G**), and actually diminished the separation of the 50-100% A β 42 fibrils. If reliable, this could indicate that the preferred A β 42 conformation actually dominates the seeding of the mixed fibrils, yielding fibrils more similar to A β 42 than to A β 40. The stronger seeding ability of A β 42 is well documented. Unfortunately, much of the differentiation by PCA is affected by intensity differences within a fibril type, which convoluted the signal. We tried many computational strategies for omitting these intensity differences but did not succeed.

Though the initial FRET experiments were promising, the spectra—especially the relationship between BF-188 and PBB5—changed dramatically with repeated analysis. Imaging the same fibrils on different days resulted in the detection of obviously different spectra. A comparison of various experimental procedures and their resulting spectra are shown in **Table A.2**, which clearly illustrates that identical methods could lead to immensely different outcomes. To test whether this was a photobleaching effect, staining and imaging in the presence of the radical scavengers DABCO and Trolox was attempted but did not improve the consistency of the spectra. Suspension of the fibril aggregated in PermaFluor mountant was also tested with similar results.

By the conclusion of this portion of the study, the cause of the inconsistent spectra was not determined. Photobleaching protectant, dye wash-out, delay time before staining, delay time before imaging, laser power used, and the total amount of laser exposure time all had no consistent effect on the strength (or lack) of FRET observed. Thus, dye degradation, photobleaching, and temporal changes in relative binding affinity or binding modes all seem unlikely culprits of the inconsistency. Because we had exhausted all these hypotheses, we began focusing more effort on using lifetime data rather than spectral data in our analyses.

FLIM can be used to further discriminate mixtures

To initially test which dyes would have fluorescence lifetime sensitivity to the different A β fibril types, aggregates were stained with one dye at a time and their fluorescence lifetimes analyzed using FLIM. Lifetimes are highly sensitive to local environment and are not dependent on the amount of labelled material, thus potentially increasing the amount of discriminatory power of the method. We found that dyes that had provided little spectral discrimination between A β 40 and A β 42 had measurable differences in lifetimes. Example data is shown for the dye CRANAD-44 (**Figure 1.3**). The mean lifetime, individual lifetime components, and the ratio of amplitudes of the decay components may all be different when bound to different fibrils. Though not shown here, CRANAD-3, THK-265, and PBB5 were also tested and had promisingly disparate lifetime attributes.

The work on FLIM was cut short by the transition of effort to that presented in Chapter 2. However, there are still great strides to be made in the realm of FLIM and amyloid polymorphs. The sensitivity and specificity of the method are unparalleled. The drawback of this approach is that photon detectors with high enough resolution to detect the differences observed here are

expensive and rare. To achieve the ultimate goal of polymorph fingerprinting for the high-throughput evaluation of diverse samples, a dependency on lifetime may be less desirable for this reason. However, if data obtained in this way could be both more reliable than spectral information and more straightforward than through high-resolution structural determination techniques, it would be a major step toward high-throughput amyloid fingerprinting. The key for anyone working on this in the future will be to obtain enough biological replicates to achieve statistical significance in consistent differences among polymorphs. Without it, such a method will not be a reliable tool.

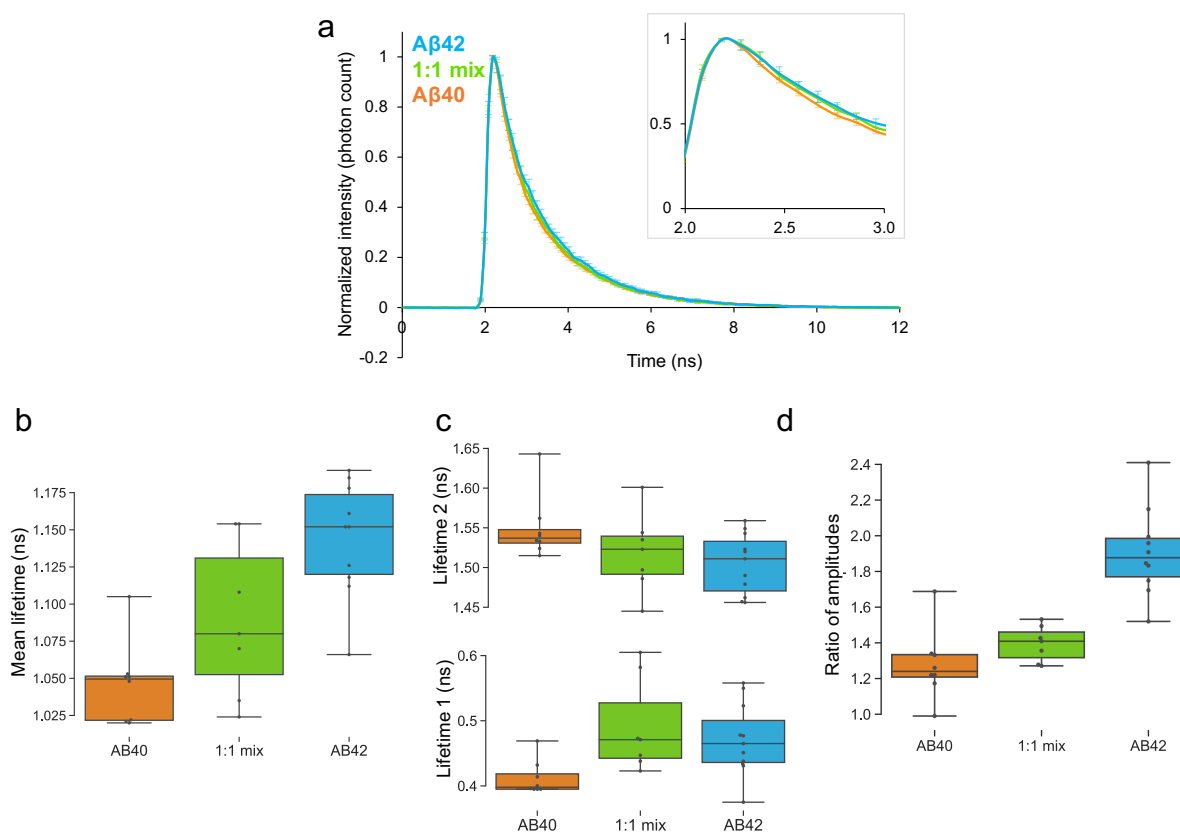


Figure 1.3. FLIM discriminates between fibrils composed of different ratios of A β 40 and A β 42. Aggregates of fibrils made from synthetic peptides in 1:0, 1:1, or 0:1 ratios of A β 40:A β 42 were embedded in agarose gel and stained with 5 μ M CRANAD-44. A Leica SP8 FLIM-STED confocal microscope was used to excite the dye at 470 nm. Built-in software was used to calculate lifetimes using 2 exponentials. **(A)** Decay curves, with initial decays shown in the inset. **(B)** Mean fluorescent lifetimes. **(C)** Lifetimes 1 and 2. **(D)** Ratio of amplitudes.

AFM may be able to pull on fibrils, but troubleshooting is still required

To initially test whether an AFM tip could be used to pull apart an amyloid fibril, we synthesized a Zn^{2+} catalytic amyloid, functionalized a portion with maleimide, and fibrillized them. A characterization of the DBCO-derivatized peptide product is shown in **Figure 1.4**. The two peaks shown by analytical HPLC are the result of two conformations of sulfo DBCO-maleimide itself (**Figure 1.4C-D**). The final derivatized product was pure, with a mass of 905.8 Da (**Figure 1.4E**). Fibril formation was confirmed using by ThT (data not shown) and TEM, which showed a heterogeneous mixture of fibril types (**Figure 1.4F-I**). Such heterogeneity is somewhat expected, and incidentally could allow for multiple kinds of attachment opportunities of the fibril to the AFM substrate. These results encouraged us to move forward with AFM pulling experiments.

Attachment of the fibril to an azide-functionalized surface proved challenging. In initial attempts, we achieved rough AFM imaging of what appeared to be short fibril fragments, based on their diameter of ~ 8 nm (**Figure 1.5A-B**). Unfortunately, this apparent success was not easily repeatable, even when multiple derivatized:parent peptide ratios were tested (1:10, 1:50) at various concentrations. In attempting to attach the peptide electrostatically to the mica surface, which would ultimately be required for pulling experiments, many large amorphous clumps were detected as well as some smaller features (data not shown). The larger objects could have been aggregates of many fibrils, as they looked similar to those seen by TEM, which suggested that the smaller features may have been single fibrils or fibril fragments. When trying to probe them, however, we found that they were easily dislodged from the surface by the AFM tip. These difficulties were largely unexpected given the success of other groups in imaging amyloids by AFM.

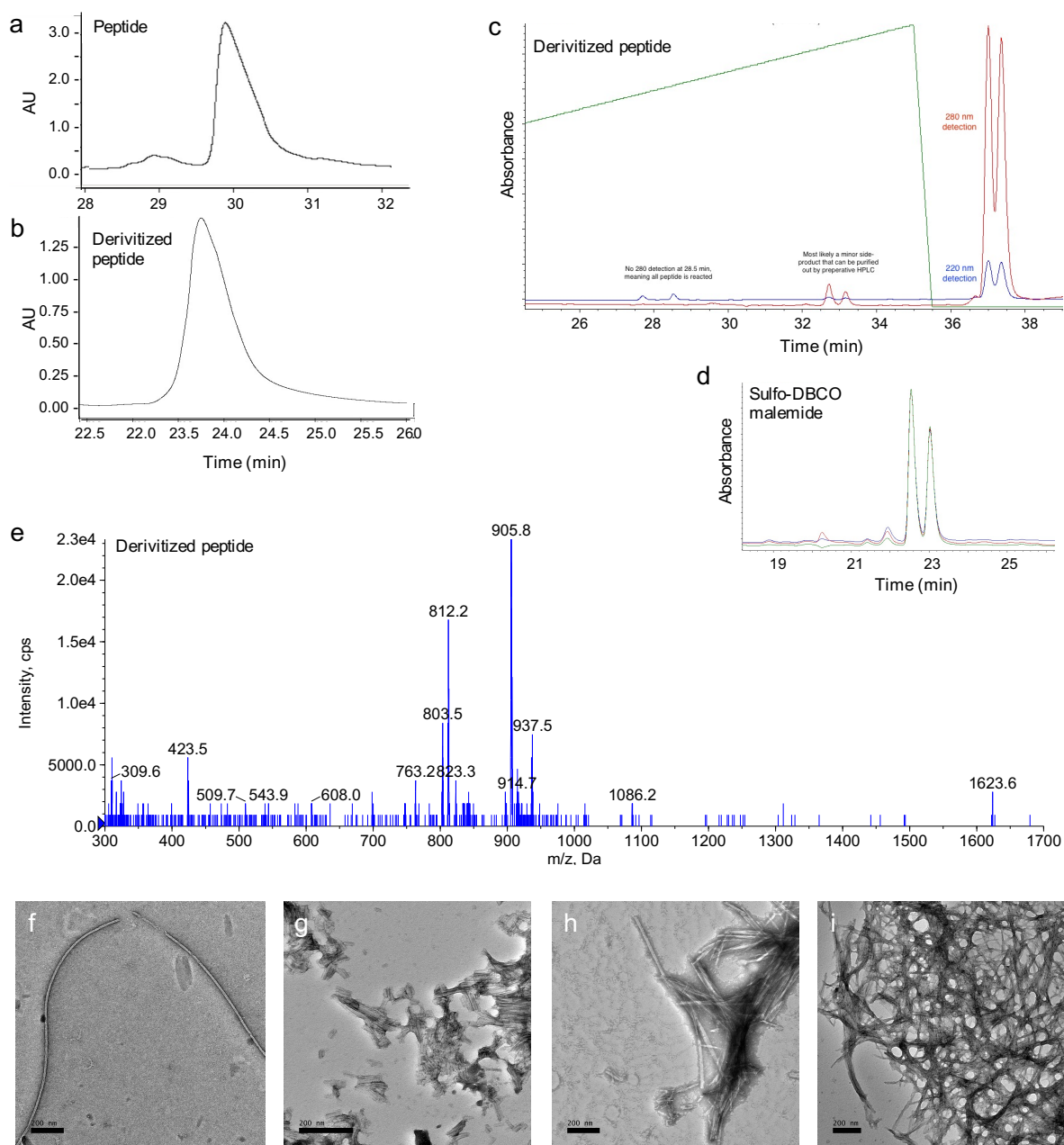


Figure 1.4. Product characterization of catalytic amyloid peptide derivitization with sulfo DBCO maleimide. (A) Peptide only, HPLC prep. 220 nm trace. Peptide elutes at 29.97 minutes. (B) Derivatized, HPLC prep. 220 nm trace. Elutes at 23.95 minutes. (C) Analytical HPLC trace of peptide + DBCO, showing its isomeric nature. The lack of 280 nm detection at 28.5 min shows that all the peptide is reacted. The peaks at ~33 min are a side product purified out by preparative HPLC. Green trace shows solvent B. (D) Analytical HPLC trace of DBCO only. 220 (blue) 255 (red) and 280 (green) nm traces. (E) Mass spectrum of derivitized and purified peptide, with a peak at *Major peak: 905.8. Expected mass: 905.6*

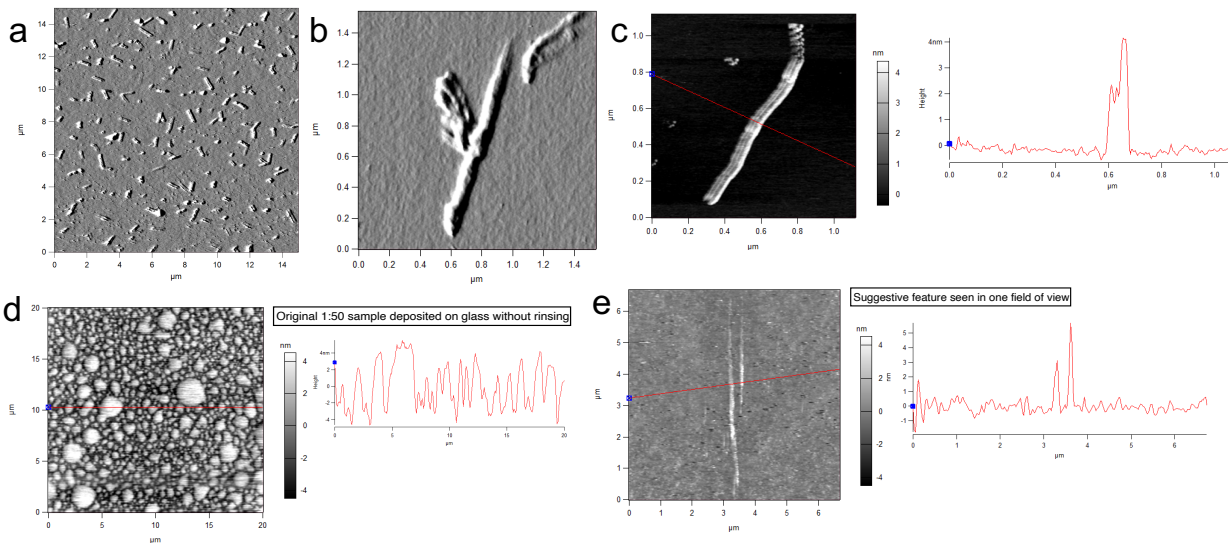


Figure 1.5. Example images from initial AFM imaging experiments. (A) 15 x 15 μm FOV showing many possible amyloid fibril fragments. 0.5 $\mu\text{g}/\text{mL}$ fibrils of 1:10 derivatized peptide were incubated overnight at 4 $^{\circ}\text{C}$ on an azide-functionalized substrate and imaged with an AFM tip. **(B)** Close-up of one example fibril with a height of ~ 8 nm. **(C)** Tiny tau adhered to a glass surface after 90 minutes of sonication. **(D)** Liquid-liquid droplets of catalytic amyloid on a glass surface. **(E)** Putative catalytic amyloid fibrils on a glass surface after rinsing.

We hypothesized that a difference in charge between our fibrils and those in the literature could cause them to have weaker nonspecific adhesion to the surface. To test the possibility that the fibrils had difficulty adhering to the mica surface due to their minimal electrostatic charge, a “tiny” R3 tau construct with a +2 charge was synthesized and fibrillized in the same manner as for the catalytic amyloid. However, only large, amorphous clumps, up to several microns in scale, adhered sparsely to the surface (data not shown). Only after aggressive 90-minute sonication was tau successfully adhered to a glass surface, again forming large, indistinct clumps. However, we did also observe two clumps that appear to consist of a small number of parallel fibrils, about 1 micron in length (**Figure 1.5C**). The scarcity of these features, however, would preclude a pulling experiment given that the functionalization of the AFM tip is degraded by prolonged contact with the surface; we would need a way to deposit the fibrils so that a significant fraction adhered to the surface. While unsuccessful in imaging or pulling, this troubleshooting effort with tau did

somewhat reassure us that inadequate surface charge was an unlikely culprit for the failed pulling experiments.

A final attempt involved returning to catalytic amyloid but deposited on a glass surface, which had seemed to work best for tau. The fact that some imaging could occur on this surface suggests that the adhesive interactions between the amyloid and the glass surface may be hydrophobic rather than electrostatic, as for mica. After absorption, the surface was covered in ~4 nm liquid droplets, which could be liquid-liquid phase-separated protein aggregates (**Figure 1.5D**). Unfortunately, after rinsing the surface with buffer, the surface was left almost completely bare, indicating that while the droplets were adhered with enough strength to be imaged, they were able to be uprooted by hydrodynamic drag. In rare exceptions, single putative fibrils were found on the surface (**Figure 1.5E**). Reconstitution of the fibrils at pH 2, on the recommendation of a colleague, did not improve fibril adhesion.

Ultimately, we concluded that it is probably not worthwhile to try to alter the surface charge of the catalytic amyloid fibril, since we have no evidence that the charged tiny tau sticks to glass any better than this uncharged peptide. However, the conditions that could possibly improve adhesion remain unclear. Optimizing adhesion conditions of better-studied amyloids such as A β may be an important first step, to understand the role of the catalytic amyloid sequence and structure itself as well as the effect of derivatization. Only then, perhaps, further experimentation with pH, charge, or fibril formation itself would prove fruitful.

Future work

All of the work presented here in Chapter 1 is unfinished. Though this is mostly due to continually encountering seemingly unsolvable problems, focusing future effort on solving a

single issue could possibly prove successful and would lead to potentially great rewards. First, in work that is likely to continue in the DeGrado lab, it would be straightforward to continue to assess the FRET capabilities of various dye combinations *in vitro*. Perhaps the spectral variation shown in **Table A.2** is unique to BF-188 or PBB5. Even if not, whatever caused the changes might not manifest in lifetime changes as well, allowing this or other dye combinations to be used in FLIM experiments. In all dye combination experiments, however, it is clearly critical to compare results obtained over time; if we had relied only upon our first experiment—even with many replicates—we would have believed that spectral differences among fibril types collected at different times would purely reflect differences among the fibrils. Determining the root cause of the observed spectral changes would also be ideal, as it may allow for this drawback to be controlled and prevented. However, no clear avenue of investigation is clear in this regard.

FLIM is certainly the most promising avenue of future research. Even in brief, preliminary experiments when testing only a few dyes, we easily observed major differences among fibril types. The potential amplification of lifetime differences in a FRET acceptor would likely increase the significance of these differences substantially. Furthermore, the single-pixel resolution of lifetime differentiation could allow for interesting comparisons of fibril morphology within a single aggregate. This methodology could be applied to the imaging of A β in senile plaques, as well, increasing the sensitivity and precision of some of the analyses presented in **Chapter 2**.

For AFM experiments, the most important next step is to establish fibril adhesion conditions that are consistent and repeatable in order to facilitate downstream analysis. We propose systematically testing different buffer salt concentrations and acidities as well as higher fibril concentrations during adsorption on the AFM substrate. Conducting these tests first with a non-derivatized version of the catalytic amyloid would be prudent. This hurdle should be able to be

overcome; we did not exhaust all of our troubleshooting options. Once accomplished, finally attempting pulling experiments to uncover the dynamics of fibrillization will be worthwhile.

1.4 REFERENCES

- (1) Barnhart, M. M.; Chapman, M. R. Curli Biogenesis and Function. *Annu. Rev. Microbiol.* **2006**, *60*, 131–147. <https://doi.org/10.1146/annurev.micro.60.080805.142106>.
- (2) Macindoe, I.; Kwan, A. H.; Ren, Q.; Morris, V. K.; Yang, W.; Mackay, J. P.; Sunde, M. Self-Assembly of Functional, Amphipathic Amyloid Monolayers by the Fungal Hydrophobin EAS. *Proc. Natl. Acad. Sci.* **2012**, *109* (14), E804–E811. <https://doi.org/10.1073/pnas.1114052109>.
- (3) Berthelot, K.; Lecomte, S.; Estevez, Y.; Coulary-Salin, B.; Bentaleb, A.; Cullin, C.; Deffieux, A.; Peruch, F. Rubber Elongation Factor (REF), a Major Allergen Component in *Hevea Brasiliensis* Latex Has Amyloid Properties. *PLOS ONE* **2012**, *7* (10), e48065. <https://doi.org/10.1371/journal.pone.0048065>.
- (4) Fowler, D. M.; Koulov, A. V.; Alory-Jost, C.; Marks, M. S.; Balch, W. E.; Kelly, J. W. Functional Amyloid Formation within Mammalian Tissue. *PLOS Biol.* **2005**, *4* (1), e6. <https://doi.org/10.1371/journal.pbio.0040006>.
- (5) Aguzzi, A.; Polymenidou, M. Mammalian Prion Biology: One Century of Evolving Concepts. *Cell* **2004**, *116* (2), 313–327. [https://doi.org/10.1016/S0092-8674\(03\)01031-6](https://doi.org/10.1016/S0092-8674(03)01031-6).
- (6) Westermark, P.; Andersson, A.; Westermark, G. T. Islet Amyloid Polypeptide, Islet Amyloid, and Diabetes Mellitus. *Physiol. Rev.* **2011**, *91* (3), 795–826. <https://doi.org/10.1152/physrev.00042.2009>.
- (7) Meade, R. M.; Fairlie, D. P.; Mason, J. M. Alpha-Synuclein Structure and Parkinson's Disease – Lessons and Emerging Principles. *Mol. Neurodegener.* **2019**, *14* (1), 29. <https://doi.org/10.1186/s13024-019-0329-1>.

- (8) Bloom, G. S. Amyloid- β and Tau: The Trigger and Bullet in Alzheimer Disease Pathogenesis. *JAMA Neurol.* **2014**, *71* (4), 505–508.
<https://doi.org/10.1001/jamaneurol.2013.5847>.
- (9) Uversky, V. N.; Fink, A. L. Conformational Constraints for Amyloid Fibrillation: The Importance of Being Unfolded. *Biochim. Biophys. Acta BBA - Proteins Proteomics* **2004**, *1698* (2), 131–153. <https://doi.org/10.1016/j.bbapap.2003.12.008>.
- (10) Kelly, J. W. The Alternative Conformations of Amyloidogenic Proteins and Their Multi-Step Assembly Pathways. *Curr. Opin. Struct. Biol.* **1998**, *8* (1), 101–106.
[https://doi.org/10.1016/S0959-440X\(98\)80016-X](https://doi.org/10.1016/S0959-440X(98)80016-X).
- (11) Bishop, M. F.; Ferrone, F. A. Kinetics of Nucleation-Controlled Polymerization. A Perturbation Treatment for Use with a Secondary Pathway. *Biophys. J.* **1984**, *46* (5), 631–644.
- (12) Sunde, M.; Serpell, L. C.; Bartlam, M.; Fraser, P. E.; Pepys, M. B.; Blake, C. C. Common Core Structure of Amyloid Fibrils by Synchrotron X-Ray Diffraction. *J. Mol. Biol.* **1997**, *273* (3), 729–739. <https://doi.org/10.1006/jmbi.1997.1348>.
- (13) Riek, R.; Eisenberg, D. S. The Activities of Amyloids from a Structural Perspective. *Nature* **2016**, *539* (7628), 227–235. <https://doi.org/10.1038/nature20416>.
- (14) Colletier, J.-P.; Laganowsky, A.; Landau, M.; Zhao, M.; Soriaga, A. B.; Goldschmidt, L.; Flot, D.; Cascio, D.; Sawaya, M. R.; Eisenberg, D. Molecular Basis for Amyloid- β Polymorphism. *Proc. Natl. Acad. Sci.* **2011**, *108* (41), 16938–16943.
<https://doi.org/10.1073/pnas.1112600108>.
- (15) Bousset, L.; Pieri, L.; Ruiz-Arlandis, G.; Gath, J.; Jensen, P. H.; Habenstein, B.; Madiona, K.; Olieric, V.; Böckmann, A.; Meier, B. H.; Melki, R. Structural and Functional

- Characterization of Two Alpha-Synuclein Strains. *Nat. Commun.* **2013**, *4*, 2575.
<https://doi.org/10.1038/ncomms3575>.
- (16) Goldsbury, C.; Frey, P.; Olivieri, V.; Aebi, U.; Müller, S. A. Multiple Assembly Pathways Underlie Amyloid- β Fibril Polymorphisms. *J. Mol. Biol.* **2005**, *352* (2), 282–298.
<https://doi.org/10.1016/j.jmb.2005.07.029>.
- (17) Greenwald, J.; Riek, R. Biology of Amyloid: Structure, Function, and Regulation. *Structure* **2010**, *18* (10), 1244–1260. <https://doi.org/10.1016/j.str.2010.08.009>.
- (18) Dunstan, D. E.; Hamilton-Brown, P.; Asimakis, P.; Ducker, W.; Bertolini, J. Shear-Induced Structure and Mechanics of β -Lactoglobulin Amyloid Fibrils. *Soft Matter* **2009**, *5* (24), 5020–5028. <https://doi.org/10.1039/B914089A>.
- (19) Rambaran, R. N.; Serpell, L. C. Amyloid Fibrils. *Prion* **2008**, *2* (3), 112–117.
<https://doi.org/10.4161/pri.2.3.7488>.
- (20) Condello, C.; Maxwell, A. M.; DeGrado, W. F. Structural Homogeneity and Inter-Subject Variability in Familial and Sporadic Alzheimer’s Disease; Dominant Seeding of Mutant AB Prions. *Submitt. PNAS* **2017**.
- (21) Yu, H.; Siewny, M. G.; Edwards, D. T.; Sanders, A. W.; Perkins, T. T. Hidden Dynamics in the Unfolding of Individual Bacteriorhodopsin Proteins. *Science* **2017**, *355* (6328), 945–950.
- (22) Lee, M.; Wang, T.; Makhlynets, O. V.; Wu, Y.; Polizzi, N. F.; Wu, H.; Gosavi, P. M.; Stöhr, J.; Korendovych, I. V.; DeGrado, W. F.; Hong, M. Zinc-Binding Structure of a Catalytic Amyloid from Solid-State NMR. *Proc. Natl. Acad. Sci.* **2017**, *114* (24), 6191–6196. <https://doi.org/10.1073/pnas.1706179114>.

CHAPTER 2

Emergence of distinct and heterogeneous strains of amyloid beta with advanced Alzheimer's disease pathology in Down syndrome

ABSTRACT

Strains of amyloid beta ($A\beta$) can have varying pathogenicity and may underlie the phenotypic heterogeneity of Alzheimer's disease (AD). Understanding how $A\beta$ strains may differ with progressing disease is critical for developing effective AD therapies. Here we interrogate $A\beta$ strain differences in the context of Down syndrome (DS), the most common genetic cause of AD, which provides a model for the predictable onset of the disease. We evaluated bulk neuropathology and $A\beta$ strain profiles in the post-mortem brain tissues of 210 DS, AD, and control individuals. Using conformation-sensitive fluorescent probes, we determined that AD and DS share many $A\beta$ strains in common but found unique and more heterogeneous strains in subjects with severe AD pathology. The emergence of distinct strains with advanced disease in DS suggests that the confluence of aging, pathology, and other DS-linked factors may favor conditions that generate strains that are unique from sporadic AD.

2.1 INTRODUCTION

Alzheimer's disease (AD) is a progressive neurodegenerative disease that affects 10% of the US population over 65 years of age¹ and responds only minimally to currently available therapeutics.² Most people with AD initially suffer from memory loss, apathy, and depression, followed by impaired communication and confusion, and eventually, motor debilitations that often lead to death.³ Inherited or familial AD (fAD) is early-onset but relatively rare, while the majority of cases are either associated with Down syndrome (AD-DS) or are sporadic (sAD), which is manifested by later onset and no clear genetic cause.

The AD brain is marked by an abundance of extracellular amyloid beta (A β)-rich plaques and intraneuronal neurofibrillary tangles (NFTs) composed of hyperphosphorylated tau. Both A β and tau are therefore believed to play a causative role in AD. However, the precise roles of these peptides—either independent or synergistic⁴—in its pathogenesis are unclear. A β aggregation is speculated to be the nucleating event in AD, as it accumulates in the brain 10-20 years before the onset of dementia,^{5,6} followed by tau deposition concomitant with clinical symptoms.⁷⁻⁹ The molecular genetics of AD further highlights the importance of A β in disease pathogenesis: mutations in the amyloid precursor protein (APP, from which A β is generated) or in the APP processing enzyme presenilin lead to fAD.¹⁰ Alternatively, mutations in tau lead to other types of dementias with NFT pathology.¹¹

The onset, progression, and severity of symptoms in sAD are diverse.¹² This heterogeneity is likely due at least in part to the structural diversity of A β species in the AD brain.¹³⁻¹⁵ Normal APP processing results in A β peptides of various lengths, most commonly comprising A β residues 1-40 (A β 40) and 1-42 (A β 42). These isoforms can in turn adopt a multitude of distinct molecular

conformations *in vitro*,¹⁶ form fibrils of differing structure and pathogenicity,¹⁷ and have been found as diverse ultrastructural assemblies in different clinical AD phenotypes.^{18,19} The ability of brain-derived A β fibrils to propagate their structure in a prion-like mechanism^{14,20–22} suggests that structurally distinct, self-propagating strains of A β might underlie the clinicopathological heterogeneity in sAD. Indeed, we recently showed that different A β strains differentiate plaques in fAD subtypes,¹⁴ supporting a hypothesis that individuals each have only a few of the many A β strains found across AD. Together, this evidence suggests that different molecular structures of A β have varying pathogenicity and may underlie the phenotypic heterogeneity of sAD. Understanding whether more pathogenic strains are seeded early in the disease or evolve with time and environmental changes would enable more targeted approaches to diagnostic and therapies.

Thus, robust methods of interrogating the role of A β early in AD are needed. Previous efforts have focused on fAD individuals with mutations that affect the production of A β because they cause comparable phenotypes to sAD in an identifiable, deterministic manner.²³ Such studies have yielded critical insights into the pathogenesis of AD, but as fAD represents <1% of all AD cases,²³ the size and scope of these investigations are limited. Alternatively, as the most common genetic cause of AD, Down syndrome (DS) presents promising opportunities to study the onset of AD. Due to trisomy of chromosome 21 (Chr21), which encodes *APP*,²⁴ people with DS have a lifelong overproduction of APP leading to increased accumulation of A β . AD neuropathology is prevalent in DS individuals over the age of 40,²⁵ while dementia is diagnosed in approximately 65-80% of the DS population over 65 years of age.²⁶ The distribution and biochemical composition of A β plaques and NFTs in AD-DS are similar to fAD and sAD,^{27,28} as is the progression of clinical symptoms including dementia.^{29,30} Thus, compared to the relatively rare fAD, DS offers unique advantages for comprehensive studies of AD pathogenesis.

Despite promising prospects of AD prevention trials in DS,³¹ research into the molecular pathogenesis of AD-DS has been limited by a number of obstacles. A lack of standardized collection and documentation for DS autopsy cases has restricted the size and characterization of study cohorts.³² Furthermore, due to the overexpression of APP and other Chr21 genes in AD-DS, its molecular phenotypes and mechanisms may be different from sAD. Yet the histological methods often used for assessing the distribution and morphology of A β and tau lesions in DS have often lacked the specificity to interrogate such molecular detail. PET imaging, while enabling longitudinal studies of the spread and severity of A β load in AD-DS, is also relatively nonspecific to A β morphotypes³³⁻³⁵ and primarily binds only a subfraction of A β in AD.³⁶ Clearly, there is a need for applying precise, high-resolution methods to the analysis of A β pathology in AD-DS.

Environment-sensitive fluorescent dyes such as Congo Red,³⁷ ThT,³⁸ and others³⁹ have historically been invaluable in probing A β conformation in AD. Though lacking the definitive structural detail of cryo-electron microscopy (cryo-EM) or ssNMR, dye-based analysis is high throughput while still sensitive to structural differences.⁴⁰ Of further advantage, it can be performed *in situ*, without the need for stringent purification. We previously optimized a set of three dyes, BF-188, FSB, and curcumin, to discriminate amyloid deposits in post-mortem fAD and sAD tissue and identified distinct A β strains within individuals.¹⁴ Because differences in fibril conformation, isoform composition, density, and other local environmental factors can all impact a plaque's fluorescence signature, they contribute to the definition of different strains in this context.

Here we apply this method in the first comparative analysis of A β strains among plaques in 210 individuals with DS or AD as well as in control subjects. We sought to identify whether a distinct subset of A β strains are present before the onset of dementia in AD and how such strains

might change or persist throughout the disease. Using principal component analysis (PCA) on the fluorescence spectra of dyes bound to intact plaques, we found that most strains of A β appear to be common to sAD and AD-DS. However, some DS individuals with the most severe neuropathology additionally present with some distinct strains. These differences are partially but not fully explained by the bulk amount of A β 40 and A β 42 in each tissue and may be related to a two-fold elevation of phospho-Tau (pTau) in our AD-DS cohort. We posit that the increasingly divergent biochemical environment of the aging DS brain may be able to foster the propagation of unique strains of A β not otherwise found in AD.

2.2 METHODS

Cases

Deidentified post-mortem brain tissue was obtained from 210 individuals: 152 DS (+/- AD), 34 AD without DS, and 24 control cases without cognitive impairment but with AD neuropathological change (ADNC). Details on each case are outlined in **Table C.1**. Included in the DS cohort is one subject with partial trisomy of Chr21 (PT21) that does not include *APP*, which resulted in normal aging without dementia⁶³ and affords us interesting comparisons between characteristics that might differ in DS without the eventuality of AD. Frozen blocks and/or formalin-fixed paraffin-embedded (FFPE) sections were analyzed from the frontal cortex. Note that not all cases were able to be used for every experiment, depending on amount and type of tissue preparation available for each case (see **Table C1**). All cases able to be used in an experiment are included in the presented results unless otherwise specified.

Immunohistochemistry (IHC)

Deparaffinized fixed sections were pretreated in 98% formic acid for 6 min to enhance immunoreactivity. After blocking with 10% normal goat serum (ngs) in PBS with 0.2% Tween 20 (PBST), sections were incubated at room temperature in primary antibodies overnight followed by secondary antibodies for 2 h. Primaries were prepared in 10% ngs and applied as combinations of either: anti-A β 1-40 rabbit polyclonal (Millipore Sigma #AB5074P, 1:200) and anti-A β 1-42 12F4 mouse monoclonal (Biolegend #805502, 1:200); or anti-A β 17-24 4G8 mouse monoclonal (Biolegend #800709 1:1000) and anti-tau (phospho-S262) rabbit polyclonal (Abcam #ab131354, 1:200). Polyclonal IgG H&L secondaries were Alexa Fluor 488- and 647-conjugates (Thermo Fisher #s A11029, A21235, A11008, and A21244) applied 1:500 in 10% ngs in PBST.

Stained slides were scanned on a ZEISS Axio Scan Z1 digital slide scanner at 20x magnification. Excitation at 493, 553, and 653 nm was followed by detection at 517 nm (A β 40 or pTau), 568 nm (autofluorescence), and 668 nm (A β 42 or tau).

Neuropathological scoring

To determine the level of AD pathology at the time of death, one IHC-stained fixed cortical section was evaluated for each case. The number of A β 40- and A β 42-positive plaques, neuritic plaques, and phospho-S262-positive NFTs were averaged among three random 1-mm² sections of grey matter. A β and tau scores were assigned according to the criteria in **Table 2.1**, which were formulated to honor traditional staging methods, to allow for scorer efficiency, and to separate the patient pool into large enough groups to facilitate downstream analysis. Importantly, the relationship between NFT quantity and cognitive impairment in AD is well established,⁴⁵ enabling a rough assessment of each case's likelihood of symptoms at the time of death.

Table 2.1. A β and tau scoring criteria by number of pathological feature density. Frontal cortical tissue sections were stained for A β 40, A β 42, and pTau by IHC. The number of pathological features was counted and averaged across three random 1-mm² sections of grey matter.

X	A β	Tau
0	<1 plaque/mm ²	<1 mature NFT/mm ²
1	<1 dense-cored plaque but ≥ 2 total plaques	1-5 NFTs
2	≥ 1 dense-cored but <2 neuritic plaques	5-12 NFTs
3	≥ 5 dense-cored and 2-15 neuritic plaques	12-25 NFTs
4	≥ 15 neuritic plaques	≥ 25 mature NFTs

NFT accumulation in the neocortex (Braak stage V-VI) is required for a post-mortem diagnosis of AD. Therefore, to cross-check any assignment of $X_{\text{tau}}=0$ in AD, a BF-188-stained fixed section was viewed with a red-light filter by confocal microscopy, which would reveal both phosphorylated and unphosphorylated tau species⁵⁵. We eliminated from downstream analysis AD cases that indeed appeared to have no NFTs (n=2) in the frontal cortex.

DNA extraction and genotyping

Upon receipt, frozen brain tissue was homogenized in PBS and stored 10% w/v in PBS at -80 °C until thawed on ice for biochemical assays. Genomic DNA was purified from this homogenate using a DNeasy Blood & Tissue Kit (Qiagen cat #69506).

To determine the *APOE* genotype of each case, gene fragments encompassing the two *APOE*-relevant SNPs were amplified by PCR based on the protocol described by Zhong et al. 2016.⁷³ Each 50- μ L reaction contained 1 U Phusion Plus DNA Polymerase, 200 μ M dNTPs, 1X Phusion GC buffer, 5% DMSO, 0.2 μ M forward and reverse primers, and 10-100 ng gDNA. Primer sequences and cycling conditions are in **Table B.3**. Purified PCR products were Sanger sequenced by Genewiz (San Francisco, CA).

Protein quantification

To determine the total concentration of soluble APP and tau present in each frontal cortex sample, sandwich enzyme-linked immunosorbent assays (ELISAs; Invitrogen, cat #s KHB0051 and KHB0041) were performed on brain homogenate (10% in PBS, called “10% BH”) clarified through centrifugation to remove cell debris and the majority of insoluble proteins. Samples were prepared and stored in low-binding 96-well plates and measured according to manufacturer directions. It should be noted that a subset of samples from two tissue banks were measured separately in time and were found to have 10-100x less soluble tau than the lowest other sample; this set of samples was not included in any bulk analyses on the assumption of batch error. Protein concentrations were normalized to total brain protein in the clarified homogenate as determined by a bicinchoninic acid (BCA) assay.

Insoluble protein fractions were extracted from brain homogenate by sonicating 10% BH with 75% v/v formic acid for 20 min followed by ultracentrifugation at $48000 \times g$ for 1 h at 4 °C. The supernatant was neutralized with 20-fold dilution in neutralization buffer (1M tris base $[\text{NH}_2\text{C}(\text{CH}_2\text{OH})_3]$ 0.5M $\text{Na}_2\text{HPO}_4 \cdot 7\text{H}_2\text{O}$, pH 10.5) and was stored in aliquots at -80 °C until use. To measure concentrations of A β 40, A β 42, and insoluble tau species in these extracts, ELISAs were attempted but were abandoned due to the imprecision of biological replicates. Therefore, homogeneous time-resolved fluorescence (HTRF) assays were performed instead. Total tau (Perkin Elmer Cisbio 64NTAUPEG), tau phospho-S202/T205 (64TS2PEG), A β 40 (62B40PEG), and A β 42 (62B42PEG) HTRF kits were used according to manufacturer protocols. Peptide standards were not provided in either tau kit for generating standard concentration curves, so unphosphorylated and hyperphosphorylated 0N4R tau from insect cell expressions (gifts from Aye Thwin and Dr. Greg Merz, UCSF) were used after optimization of standard concentration ranges.

Spectral profiling of plaque-bound fluorescent dyes

Cases with $X_{A\beta}=0$, including the PT21 case, could not undergo $A\beta$ strain analysis due to their lack of plaques. For cases with sufficient pathology, adjacent cortical sections were blocked in PBST, stained with 2.5 μ M curcumin, BF-188, and FSB prepared in PBS (with 5% EtOH for curcumin), and washed in PBS. Labelled plaques were imaged in the spectral (Λ) scan mode of a Leica SP8 confocal microscope using a 40x water immersion lens (1.1 NA), a 405-nm laser for excitation, and a HyD detector at 512- \times 512-pixel resolution. For each field-of-view, the optical plane was moved to the center of the z-stack volume for a given $A\beta$ deposit, and fluorescence emission was acquired from a series of 40-image steps spanning 385- to 780-nm wavelengths using a sliding 15-nm-wide detection window.

Micrographs were analyzed using custom MATLAB software⁷⁴. Plaques were automatically segmented based on size and fluorescence intensity. False-positive objects, including neuritic plaque-associated NFTs, were manually excluded to ensure that fluorescence information was plaque-specific. Separate spectra obtained from each of the three dyes were normalized to their maximum intensities and randomly concatenated to form the full 1200-nm spectral vector for each patient case used in PCA. To avoid biasing PCA towards individuals with more plaques, we limited the analysis to 30 randomly-selected vectors per patient. We compared multiple under-sampled PCA to each other and to PCA that included all possible vectors to ensure that the trends observed in each were the same.

PCA and statistical analysis

PCA was performed on composite spectral vectors using the Python sklearn decomposition package. Comparisons made between groups were always performed in the same eigenspace. Density contours were applied to the PCA plot using the matplotlib contour function calculated on a Gaussian kernel density estimation (KDE) mesh grid within the Scipy stats package. To account for the overrepresentation of DS cases in our analysis, we validated our PCA through computational oversampling of young DS cases as well as through the inclusion of all (>30) spectra from the given AD cases, neither of which altered the relationships among samples in principle component (PC) space.

To determine the heterogeneity of strains, the weighted root-mean-square deviation (RMSD) of spectral vectors in PCs 2, 3, and 4 was calculated for each patient and for each cohort using the following equation:

$$\sqrt{\frac{\sum_{i=1}^N d_i^2}{N-1}}, \text{ where } d_i = \sqrt{(x_i - \bar{x})^2 w_x^2 + (y_i - \bar{y})^2 w_y^2 + (z_i - \bar{z})^2 w_z^2}.$$

Per-patient calculations were performed on each patient vector with N as the total number of patient spectral vectors and the barred coordinates representing the patient centroid. Per-cohort calculations were calculated on the centroid of each patient in the cohort with N as the total number of patients in the cohort and the barred coordinates representing the cohort centroid. The weights are the proportion of overall variance explained by PCs 2, 3 and 4.

Linear regression from SciPy and the StatAnnot package were used to determine significance of relationships between PCA coordinates and numerical and categorical case attributes respectively. One-way multivariate analysis of variance (MANOVA) was performed on

the centroids of each patient in PC2 and PC3 to determine the resolving power of PCA among groups.

2.3 RESULTS

AD pathology varies by age and cohort

We first sought to characterize the key biological and genetic attributes of the cases in our study to allow us to later control for potential covariates in our analysis of A β strains. The age distributions of the three main cohorts—DS (including AD-DS), AD (without DS), and ADNC—are shown in **Figure 2.1A**. We prioritized obtaining and analyzing DS cases under 40 years of age, since these were the most likely to provide insight into pre-clinical AD. Though such cases are relatively rare, we obtained 21 cases between 20-40 years of age, making this the largest study of young DS post-mortem tissue to date in addition to the largest known cohort of DS generally in a molecular study of A β . The majority of our DS cases were aged 35-65 years at the time of death,

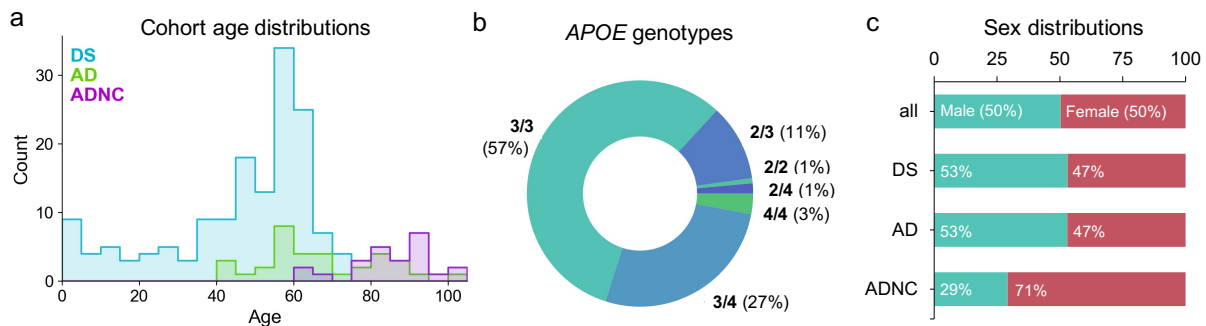


Figure 2.1. A range of case ages, genotypes, and sexes comprise the study cohorts. (A) Per-cohort distributions of patient ages at death ($n_{DS}=152$, $n_{AD}=34$, $n_{ADNC} = 24$) **(B)** Proportion of cases with each *APOE* genotype, when known ($n=137$). Genotypes were established through Sanger sequencing of SNP-containing *APOE* amplicons purified from gDNA. **(C)** Percent of all cases and of each cohort that were known to be male or female ($n=204$).

while most AD cases tended to be older (aged ~55-90 years); generally, these two groups are considered comparable because of accelerated aging in DS. Fifty percent were male and 50% female (**Figure 2.1C**).

We chose to genotype our samples for *APOE*, a gene encoding the cholesterol transport and lipid metabolism protein apolipoprotein E (apoE), because its three isoforms ($\epsilon 2$, $\epsilon 3$, and $\epsilon 4$) are linked to varying AD severity.⁴¹ The $\epsilon 4$ allele is strongly associated with earlier onset of dementia in both DS⁴² and the general population.⁴³ Genotyping revealed a majority of cases as *APOE* 3/3, with 43 cases having at least one $\epsilon 4$ allele (**Figure 2.1B**). For the subset of cases for which *APOE* was provided by the tissue bank, 90% of genotypes matched those established by our method (data not shown).

An additional source of variation in our cohorts stems from the fact that the tissue for this study was sourced from eleven different brain banks and spanned nearly four decades of collection (see **Table C.1**). As a consequence, the methods and timing of tissue fixation and storage post-mortem, as well as the methods and quantity of clinical analyses and neuropathological assessment at autopsy, varied greatly across our 210 samples. To obtain a standardized measure of AD neuropathology, we generated our own pathological scores based on $A\beta$ ($X_{A\beta}$) and tau (X_{tau}) load in the frontal cortex detected using antibodies targeting $A\beta 40$, $A\beta 42$, and phosphorylated tau, as outlined in **Table 2.1**. Examples of the appearance of $A\beta$ and tau pathology in cases assigned $X_{A\beta}$ and X_{tau} 1 and 4 are shown in **Figure 2.2A**.

Our standardized method allows for direct, consistent comparisons of neuropathology among cases for this study. It is important to note that the absence of tau in the particular tissue section we studied does not preclude its presence elsewhere in the brain, nor are we diagnosing AD with this method. However, because tau accumulation is associated with the onset of

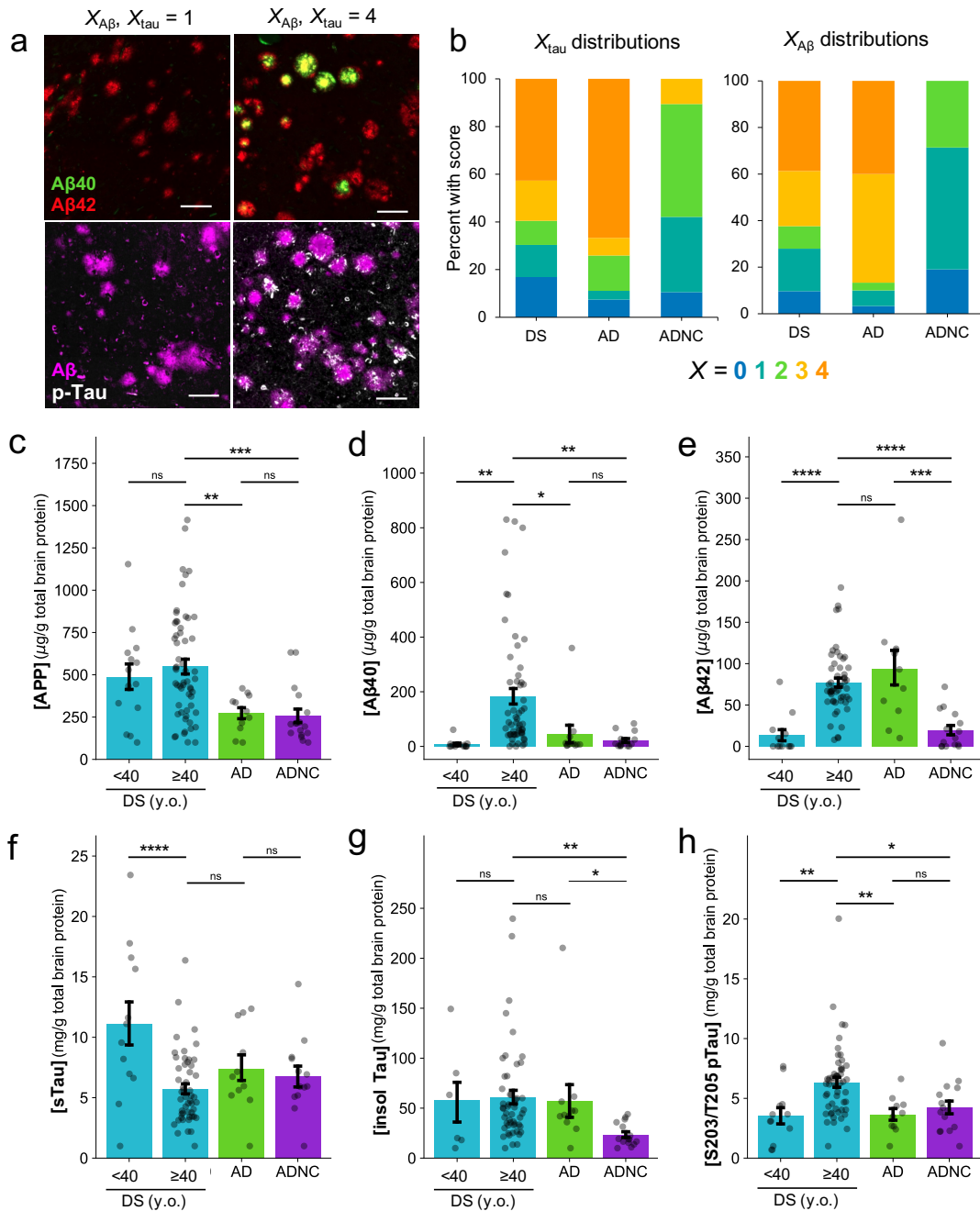


Figure 2.2. Characterization of neuropathology using custom histological scoring and biochemistry. (A) Representative IHC images from a DS case with $X_{\tau} = 1$ and $X_{\beta} = 1$ (UCI 35-06) and from a DS cases with $X_{\tau} = 4$ and $X_{\beta} = 4$ (UCI 29-06). FFPE sections were dual stained with primary antibodies specific for either A β 40/A β 42 or total A β /S262 pTau and were detected using fluorescent secondary antibodies. Scale bars are 100 μ m. (B) Proportions of cases in each cohort with each X_{β} and X_{τ} as determined by custom manual scoring methodology. (C-H) Protein concentrations determined in frozen tissue, \pm SEM. For soluble proteins (APP, sTau), clarified brain homogenate was assayed by ELISA. For insoluble proteins (A β 40, A β 42, total insoluble tau, and pTau), formic acid-extracted samples were assayed by HTRF. Significance values were determined by student's two-tailed t-test. *: $0.01 < p \leq 0.05$; **: $0.001 < p \leq 0.01$, ***: $0.0001 < p \leq 0.001$.

dementia^{8,9,44} and post-mortem NFT density has been shown to correlate with pre-mortem cognitive scores,⁴⁵ we interpret higher X_{tau} to correspond to a greater likelihood of having had clinical symptoms of AD at the time of death. Specifically, we considered X_{tau} to indicate subjects who more likely did not experience clinical symptoms of AD during life ($X_{\text{tau}}=0$) and those who likely did ($X_{\text{tau}}=4$). This strategy enabled downstream comparisons of A β strains in DS versus probable AD-DS.

The proportions of cases with each A β and tau score are shown in **Figure 2.2B**. The majority of DS and AD cases were $X_{\text{A}\beta}$ and $X_{\text{tau}} \geq 3$, corresponding to the presence of many cored and neuritic plaques and NFTs, whereas ADNC cases tended to have less pathology ($X_{\text{tau}} \leq 2$). Within DS, both $X_{\text{A}\beta}$ and X_{tau} tended to increase with age ($R^2_{\text{XAB}}=0.61$, $R^2_{\text{Xtau}}=0.52$, $p < 0.001$), with the earliest signs of A β pathology visible in a 9-year-old with DS and of tau pathology in a 19-year-old with DS (**Figure B.2A**). Importantly, 9 DS cases had $X_{\text{tau}}=0$ with $X_{\text{A}\beta} \geq 1$. Being the most likely to be associated with pre-clinical AD, the plaques in these cases were prioritized for later A β strain assessment. The oldest DS cases without any sign of A β or tau pathology were aged 27 and 51 years, respectively. No significant trends in $X_{\text{A}\beta}$ and X_{tau} were observed relative to age among AD or ADNC cases.

Concentrations of APP and some A β and tau species differ among cohorts

We sought to characterize the amount of soluble APP in each sample in order to better understand how the processing of the protein might differ with age in DS. We also analyzed the amounts of various A β and tau peptides to bolster our neuropathological cohort comparisons and to assess potential novel trends in DS. The concentrations of APP, A β 40, A β 42, soluble tau, total tau, and S202/T205 pTau determined by ELISA and HTRF are shown in **Figure 2.2C-H**. On

average, APP in DS was 2x higher than in AD or ADNC cases (**Figure 2.2C**, $p < 0.01$ and $p < 0.0006$ by student's two-tailed t-test), which was unsurprising given its overexpression in DS. On average, A β 40 and A β 42 were 10x and 3x higher in DS individuals over 40 years of age compared to younger individuals (**Figure 2.2D-E**). By IHC, we determined that many cases with the highest A β 40 levels also had significant vascular A β 40 due to cerebral amyloid angiopathy (CAA, data not shown). However, the overall 4x elevation of A β 40 in DS individuals over 40 years of age compared to AD was not consistently explained by CAA, suggesting altered APP processing favoring A β 40 or shifted targeting of A β 40 to plaques in AD-DS.

Soluble tau concentrations were highest in the very youngest DS cases (0-2 years of age) and steadily decreased with patient age until after age 30 ($R^2=0.42$, $p < 0.0001$; **Figure B.3C**), but on average were not significantly different to those in AD or ADNC (**Figure 2.2F**). Total insoluble tau was significantly lower in ADNC than in DS, as we expected from those cases in which neuropathology was generally less severe by IHC. However, insoluble pTau species have been shown to be one of the strongest predictors of disease severity in sAD and fAD.^{4,46} We found that pTau was only significantly higher than in either AD or ADNC in DS subjects over 40 years of age (**Figure 2.2H** and **Figure B.3B**), potentially indicating more accelerated disease progression in DS.

DS individuals develop unique strains of A β with advanced AD, which differ in amounts of some tau and A β species

Environment-sensitive fluorescent dyes are ideal sensors for amyloid conformation because even small changes in local environment are exhibited in their emission spectra. While many such probes have been developed, we previously found a set of three dyes to sufficiently

discriminate between AD-relevant A β strains in situ.¹⁴ We used this same set to examine the strains in this study, with optimized computational analysis (**Figure 2.3A**). Comparing these plaque-bound fluorescence spectra by PCA allowed us to identify structural differences between strains in high throughput (**Figure 2.3B-E**). Principle component 1 (PC1) represented 62% of the variation in the spectra, which was found to be due to a shelter-in-place-related microscope calibration change. We thus focused our analyses on PCs 2 and 3, which contained an additional 20% of the spectral variation. All three dyes contributed to the assessment (**Figure B.4**). Using one-way MANOVA performed on patient centroid coordinates in PC2 and PC3, we determined that AD, DS, and ADNC are moderately but significantly differentiated by PCA (Wilks' lambda [Λ]=0.74, $p < 0.005$). AD-DS and DS in the absence of AD (here defined as $X_{\text{tau}} \leq 2$) were similarly discriminated ($\Lambda = 0.69$, $p < 0.005$). This suggests that some the most prevalent A β strains in each stage of disease may be distinct.

We defined two subsets of the eigenspace using a KDE calculated on either all ADNC vectors or all AD vectors (**Figure 2.3F**). The overlap of the densities defines a region that contains plaques from all 3 cohorts. Considering that >95% of ADNC vectors are found in this region, these vectors could represent strains of A β that are found in normal, healthy aging, and could be less pathogenic. Interestingly, vectors from DS individuals aged 30-65 years, but not <30 years ($n=3$), are all found in this region, as are vectors from DS with both low ($X_{\text{tau}}=0-2$) and high ($X_{\text{tau}}=4$) AD pathology. The plaques not within these AD or ADNC densities indicate strains which, by the resolution of our method, are found exclusively in DS. These strains were found exclusively in individuals with high levels of pathology ($X_{\text{tau}} \geq 3$).

In performing linear regression on patient centroids in each PC, we determined that the distribution of patients in PC2 is somewhat correlated with HTRF-measured A β 42 concentration

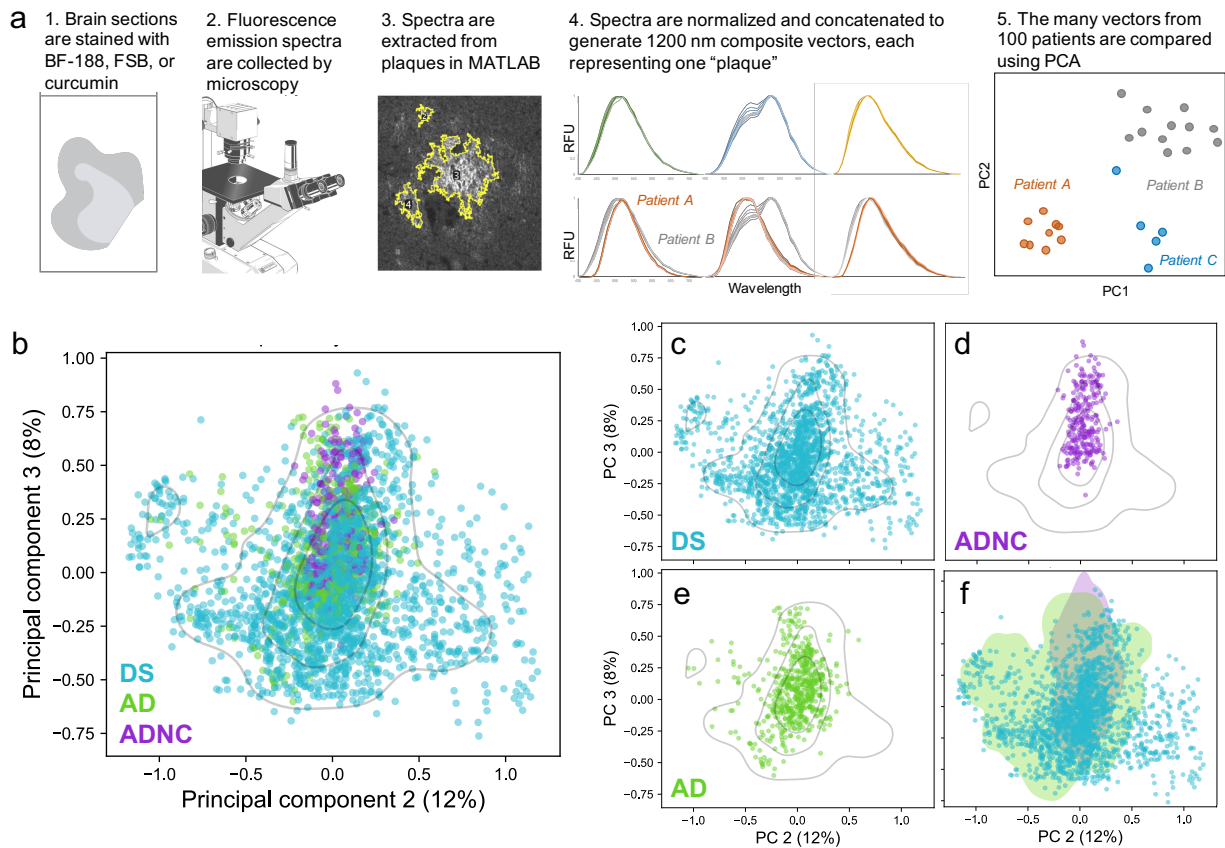


Figure 2.3. PCA performed on plaque-derived fluorescence spectra reveals a subset of conformational space unique to DS. (A) Overview of the experimental and computational workflow. (B) 2673 spectral vectors from 100 DS, AD, and ADNC cases were analyzed by PCA and are plotted in the eigenspace defined by PC2 and PC3. Each data point is the concatenated spectra of 3 dyes and represents one plaque. A Gaussian KDE is shown at 30%, 60%, and 90% probability intervals. (C-E) The PCA data are plotted separately by cohort for clarity. (F) A 99.5% KDE computed on either all ADNC vectors (purple) or all AD vectors (green) is shaded. The non-overlapping subset of DS vectors (blue points) indicate A β strains that may be unique to DS.

($r=0.34$, $p<0.05$) in DS, whereas PC3 is significantly correlated with A β 40 concentration ($r=-0.36$, $p<0.005$) when considering all patients. Alternatively, the concentrations of soluble, total, or pTau species did not significantly impact vector distributions in the eigenspace, nor did patient sex, age, or the tissue's post-mortem interval (PMI) or source bank.

Strain heterogeneity increases with pathology in DS

We previously observed in sAD and fAD patients that the heterogeneity of A β strains varies both between populations and individuals.¹⁴ We were therefore curious how heterogeneous A β strains are in DS compared to sAD and ADNC individuals. To get an overall measure of the spread of patients in each cohort, we calculated variance-weighted RMSDs of the distances of each patient centroid to the cohort centroid. We found that DS patients were more heterogeneous (RMSD = 0.055) than AD patients (RMSD = 0.030), which were more heterogeneous than ADNC patients (RMSD = 0.023) in this eigenspace, perhaps suggesting a greater difference in A β strains among DS individuals than among others.

Examples of per-patient vector populations are shown in **Figure 2.4A**. To quantify per-patient heterogeneity, we also calculated the RMSD of the distances of the patients' vectors to their centroid. We found that like previously seen in fAD, per-patient RMSDs varied widely between patients but that strains were generally more homogeneous within a patient than for the entire population. In general, ADNC individuals were more homogeneous than AD cases, which were more homogeneous than DS cases (**Figure 2.4B**). The proportion of DS cases with high RMSD were substantially greater in cases with advanced disease ($X_{\text{tau}}=3$ or 4; **Figure 2.4C**) and age (**Figure B.5A**). This suggests that the continued accumulation of A β in DS may result in its adoption of new or additional conformations. The presence of two APOE $\epsilon 4$ alleles, but not patient sex, also contributed to heterogeneity (**Figure B.5B-C**).

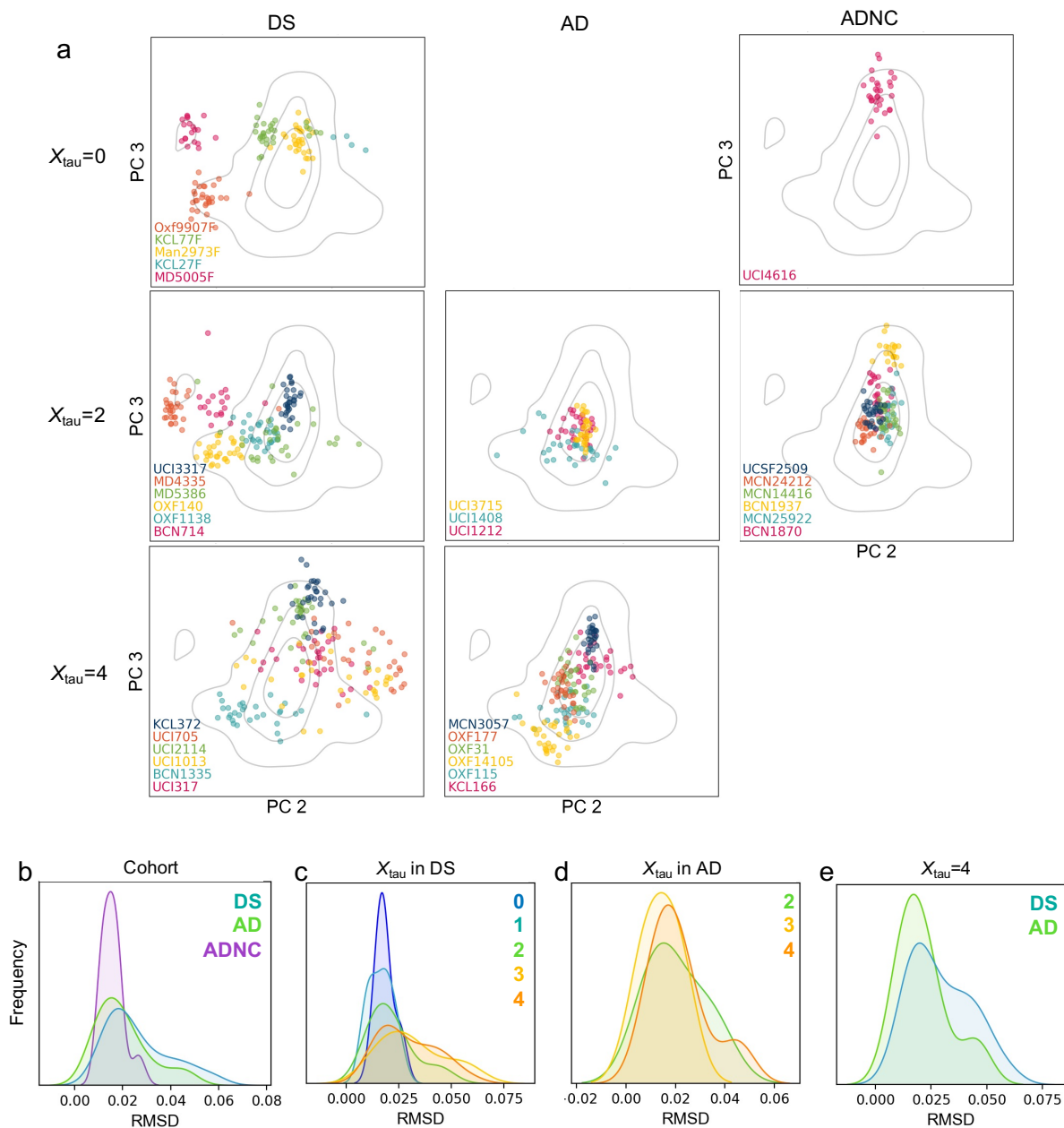


Figure 2.4. Per-patient strain heterogeneity increases with advancing pathology. (A) Examples of per-patient vector distributions in PC space. The columns show plots of DS, AD, and ADNC cases respectively. The rows show plots of cases with different X_{τ} in each cohort, when such cases exist. Each point is the spectral vector representing a single plaque from a given patient. (B-E) KDEs of RMSDs calculated using each case's vector distributions in PCs 2-4. These distributions are compared between (B) cohorts, (C) X_{τ} in DS, (D) X_{τ} in AD, and (E) AD and DS cases with $X_{\tau}=4$.

2.4 DISCUSSION

Key neuropathological and biochemical differences distinguish AD-DS from sAD

Quantifying the progression of neuropathological hallmarks of sAD and AD-DS is critical for a comprehensive understanding of how A β and tau species might contribute—either independently or interactively—to the development of disease in each population. In DS, A β accumulation is known to begin in the late teenage years in the temporal lobe, with pathology developing throughout the brain in a similar pattern as in sAD by age 55.²⁸ By IHC, we observed the earliest signs of A β deposition in DS as diffuse A β 42 in the frontal cortices of individuals just younger than 10 years of age. In agreement with established trends,^{47–49} A β 40 and A β 42 both generally increased with age across the DS population, though A β 40 was always found in the presence of appreciable A β 42 accumulation. However, by HTRF, only A β 40 and not A β 42 levels were significantly elevated in DS over 40 years of age.

We also found slightly elevated levels of S202/T205 pTau by HTRF in AD-DS compared to AD and ADNC, which may indicate accelerated or more severe disease in DS. It is also interesting to note that while HTRF did not unveil significant differences in this species of pTau between AD and ADNC individuals, our neuropathological scoring method, which used an antibody against S262 pTau, greatly differentiated the two cohorts. A number of differences in the preparations of the two measured materials could be responsible. However, it is also possible that the difference is a consequence of different profiles of pTau that associate differently with NFTs or disease severity in AD. Current efforts in dissecting the timing and composition of pathogenic tau⁵⁰ should certainly be expanded to include AD-DS to better understand the relationship between tau and disease.

Our finding the presence of A β in the frontal cortex as early as 9 years and some tau pathology as young as 19 years old in DS is earlier some others have reported.^{25,28,48,51} Since tau pathology does not extend beyond the temporal cortex to other regions of the cerebral cortex until Braak stage IV,⁵² it is also surprising that we found tau pathology in the frontal cortex of many cases assigned Braak stages I–III. These findings likely point to the sensitivity advantage of fluorescence-based methods over chromogenic stains. Yet overall, our neuropathological analysis highlights the heterogeneity of the DS brain, particularly in the relationships between A β and tau pathology, which do not appear to perfectly mirror that in sAD. This suggests that while on the whole AD-DS is an apt model for sAD, caution should be taken in assuming that all DS individuals are equally appropriate.

One subset of early-stage strains in DS reflect those in AD, but another subset is distinct.

Considering the failure of multiple clinical trials for AD targeting the production of A β ,⁵³ it is critical that we recognize the diversity of A β species present in the brain and understand which, if any, might be most responsible for the onset or severity of dementia. To this end, we were interested in evaluating whether a unique subset of A β strains is present at early stages of AD, and whether early-stage strains persist or evolve with time or worsening clinical condition. To assess such relationships among strains in post-mortem tissue, we used environment-sensitive dyes to probe the amyloid plaques of individuals with DS and/or AD, as well as cognitively healthy ADNC individuals. We discriminated the plaque-bound fluorescence spectra using PCA, which successfully resolved strains of A β that are present at different stages of AD progression in DS. While these probes might report on other aspects of the plaque composition or environment,⁵⁴ their

specificity for insoluble protein aggregates and sensitivity to A β structure has been well documented^{14,39,55,56} and is expected to represent the majority of spectral variation.

We found that some of the strains we observed in the frontal cortices of DS individuals with minimal to non-existent NFTs but some A β pathology, i.e. generally before the onset of clinical symptoms of AD, are distinct from strains in AD-DS. In DS cases where tau pathology was more severe, many strains appeared common to AD and AD-DS. Intriguingly, a portion of plaques in many late-stage AD-DS individuals appear distinct from any non-DS plaques, suggesting that not all strains of A β are common to the two diseases. However, these cross-sectional observations can only suggest what may be happening temporally in these individuals. Moving forward, using strain-specific imaging agents in live subjects with DS will be critical to understanding the true evolution of A β strains in AD.

While the difference in amyloid presentation in senile plaques itself may be important for the development of anti-amyloid AD therapeutics, the causes of these different strains may also inform our understand of AD in DS. For example, neuroinflammation, in particular plaque-associated microglia activation, is known to affect amyloid conformation.⁵⁷⁻⁵⁹ As the relative populations of different types of microglial cells are altered in people with DS after the age of 40,^{60,61} these changes may manifest in altered amyloid conformation. Perhaps most critically, the progressive changes in strain composition evinced by PCA may indicate that distinct strains of A β are present prior to the onset of clinical AD. It is possible that these strains persist while other strains emerge along with clinical symptoms, in which case the next obvious question arises: are these strains harmless bystanders, or are they the catalyst of disease? If the latter, it would be critical to ensure that preventative therapies and diagnostics targeted these strains.

A β strain heterogeneity increases with AD progression.

Through calculating the RMSDs of case vector distributions in principal component space, we have found that A β strain heterogeneity varies among individuals. Heterogeneity tended to be greater in individuals with more advanced AD, particularly in DS. In most of these DS individuals, we found representation of strains both common to and unique from late-stage sAD. This suggests that while many strains common to sAD and AD-DS persist throughout life, certain conditions specific to aging or pathology in DS may allow for the emergence of new strains. Recent evidence shows that while APP has a direct role in AD-related A β neuropathology,^{62,63} other genes on Chr21 also substantially impact A β aggregation in AD-DS⁶⁴. As tau is thought to interact with A β in AD,⁴ changes in tau isoform ratios and phosphorylation via Chr21-associated proteins DYRK1A^{65,66} and RCAN1⁶⁷ could also impact A β plaque composition. Our finding of enhanced pTau in DS individuals over 40 years of age supports this hypothesis. These DS-specific changes could therefore enhance this strain diversification or alter the specific strains that are favored.

The possibility that multiple distinct A β species or a spectrum of species could exist within a single patient has important therapeutic implications. For example, a changed cellular environment could favor the dominant propagation of a previously minor strain. Should this strain be particularly pathogenic and negatively impact other neuropathological or clinical outcomes, then preventing the emergence of such a strain would be of paramount therapeutic importance. In the worst-case scenario, a seemingly successful treatment aimed nonspecifically at A β could be thwarted by the evolution of drug resistant strains, as has been observed in screens against prions causing scrapie.^{68,69} Furthermore, targeting only one or a few of many pathogenic strains in a given individual could have little impact on slowing disease progression—an outcome possibly demonstrated in the failure of anti-amyloid therapies.^{53,70}

Understanding the structural characteristics of these strains in more detail will help us understand how they may evolve and what role they may play in AD in DS. Ultimately, we might not be able to treat DS as a direct model for all sAD. Instead, by understanding what features in DS might be associated with altered A β strain profiles, we could triage clinical trial candidates accordingly. Based on the findings presented here, we would suggest that DS individuals already have A β conformations or plaque environments that replicate those in AD before the onset of dementia, which can differentiate with age and advancing disease. Thus, we posit that younger, non-demented individuals with DS may be the only appropriate DS candidates for clinical trials targeting sAD, while more pathologically advanced individuals would require a separate therapeutic strategy.

Future work

Whether the unique strains developing late in AD-DS are emergent or native to the individual is still not clear. A next important step will be to assess how these strains might differ among brain regions, particularly in the hippocampus where A β is believed to spread from the neocortex.^{71,72} Machine learning could also be applied to assess morphological and intra-plaque differences in our existing micrographs in order to more robustly differentiate strains. The development of PET imaging agents that are specific to multiple distinct A β strains will certainly be needed in order to follow these potential changes longitudinally. Furthermore, the success of future AD diagnostic and therapeutic efforts against A β depends on a detailed structural understanding of these strains. Mass spectrometry and cryo-EM or ssNMR should be employed to precisely understand the commonalities between specific strains in sAD and AD-DS, and moreover what aspects of plaque composition or amyloid structure make certain strains unique.

Conclusion

This work provides the first analysis of A β strains in DS and their relevance to sAD. We showed that AD-DS generally reflects the broad neuropathological features of AD but differs significantly in A β 40 and pTau concentrations. Through molecular analysis using environment-sensitive fluorescent probes, we found that DS, AD-DS, AD, and ADNC all likely share a subset of A β strains. However, as AD progresses in DS, strains become more heterogeneous and some prominent strains tend to diverge from non-AD-like A β . We therefore suggest that AD clinical trials focus on recruitment of younger DS patients who do not yet show signs of dementia; in doing so, however, it must be recognized that more heterogeneous dominant strains of A β in AD-DS would potentially not be yet recognized. It is critical to follow this work with high-resolution structural analysis of the differences between A β strains in older and younger DS and to understand the mechanistic connections between the DS brain environment and A β heterogeneity.

2.5 REFERENCES

- (1) Hebert, L. E.; Weuve, J.; Scherr, P. A.; Evans, D. A. Alzheimer Disease in the United States (2010–2050) Estimated Using the 2010 Census. *Neurology* **2013**, *80* (19), 1778–1783.
<https://doi.org/10.1212/WNL.0b013e31828726f5>.
- (2) Kumar, A.; Singh, A.; Ekavali. A Review on Alzheimer’s Disease Pathophysiology and Its Management: An Update. *Pharmacol. Rep.* **2015**, *67* (2), 195–203.
<https://doi.org/10.1016/j.pharep.2014.09.004>.
- (3) 2020 Alzheimer’s Disease Facts and Figures. *Alzheimers Dement.* **2020**, *16* (3), 391–460.
<https://doi.org/10.1002/alz.12068>.
- (4) Nisbet, R. M.; Polanco, J.-C.; Ittner, L. M.; Götz, J. Tau Aggregation and Its Interplay with Amyloid- β . *Acta Neuropathol. (Berl.)* **2015**, *129*, 207–220. <https://doi.org/10.1007/s00401-014-1371-2>.
- (5) Thal, D. R.; Rüb, U.; Orantes, M.; Braak, H. Phases of A Beta-Deposition in the Human Brain and Its Relevance for the Development of AD. *Neurology* **2002**, *58* (12), 1791–1800.
<https://doi.org/10.1212/wnl.58.12.1791>.
- (6) Villemagne, V. L.; Burnham, S.; Bourgeat, P.; Brown, B.; Ellis, K. A.; Salvado, O.; Szoëke, C.; Macaulay, S. L.; Martins, R.; Maruff, P.; Ames, D.; Rowe, C. C.; Masters, C. L.; Australian Imaging Biomarkers and Lifestyle (AIBL) Research Group. Amyloid β Deposition, Neurodegeneration, and Cognitive Decline in Sporadic Alzheimer’s Disease: A Prospective Cohort Study. *Lancet Neurol.* **2013**, *12* (4), 357–367.
[https://doi.org/10.1016/S1474-4422\(13\)70044-9](https://doi.org/10.1016/S1474-4422(13)70044-9).

- (7) Bierer, L. M.; Hof, P. R.; Purohit, D. P.; Carlin, L.; Schmeidler, J.; Davis, K. L.; Perl, D. P. Neocortical Neurofibrillary Tangles Correlate With Dementia Severity in Alzheimer's Disease. *Arch. Neurol.* **1995**, *52* (1), 81–88.
<https://doi.org/10.1001/archneur.1995.00540250089017>.
- (8) Bejanin, A.; Schonhaut, D. R.; La Joie, R.; Kramer, J. H.; Baker, S. L.; Sosa, N.; Ayakta, N.; Cantwell, A.; Janabi, M.; Lauriola, M.; O'Neil, J. P.; Gorno-Tempini, M. L.; Miller, Z. A.; Rosen, H. J.; Miller, B. L.; Jagust, W. J.; Rabinovici, G. D. Tau Pathology and Neurodegeneration Contribute to Cognitive Impairment in Alzheimer's Disease. *Brain* **2017**, *140* (12), 3286–3300. <https://doi.org/10.1093/brain/awx243>.
- (9) Joie, R. L.; Visani, A. V.; Baker, S. L.; Brown, J. A.; Bourakova, V.; Cha, J.; Chaudhary, K.; Edwards, L.; Iaccarino, L.; Janabi, M.; Lesman-Segev, O. H.; Miller, Z. A.; Perry, D. C.; O'Neil, J. P.; Pham, J.; Rojas, J. C.; Rosen, H. J.; Seeley, W. W.; Tsai, R. M.; Miller, B. L.; Jagust, W. J.; Rabinovici, G. D. Prospective Longitudinal Atrophy in Alzheimer's Disease Correlates with the Intensity and Topography of Baseline Tau-PET. *Sci. Transl. Med.* **2020**, *12* (524). <https://doi.org/10.1126/scitranslmed.aau5732>.
- (10) Tanzi, R. E.; Bertram, L. Twenty Years of the Alzheimer's Disease Amyloid Hypothesis: A Genetic Perspective. *Cell* **2005**, *120* (4), 545–555.
<https://doi.org/10.1016/j.cell.2005.02.008>.
- (11) Goedert, M.; Crowther, R. A.; Spillantini, M. G. Tau Mutations Cause Frontotemporal Dementias. *Neuron* **1998**, *21* (5), 955–958. [https://doi.org/10.1016/S0896-6273\(00\)80615-7](https://doi.org/10.1016/S0896-6273(00)80615-7).
- (12) Lam, B.; Masellis, M.; Freedman, M.; Stuss, D. T.; Black, S. E. Clinical, Imaging, and Pathological Heterogeneity of the Alzheimer's Disease Syndrome. *Alzheimers Res. Ther.* **2013**, *5* (1), 1. <https://doi.org/10.1186/alzrt155>.

- (13) Rasmussen, J.; Mahler, J.; Beschorner, N.; Kaeser, S. A.; Häsler, L. M.; Baumann, F.; Nyström, S.; Portelius, E.; Blennow, K.; Lashley, T.; Fox, N. C.; Sepulveda-Falla, D.; Glatzel, M.; Oblak, A. L.; Ghetti, B.; Nilsson, K. P. R.; Hammarström, P.; Staufenbiel, M.; Walker, L. C.; Jucker, M. Amyloid Polymorphisms Constitute Distinct Clouds of Conformational Variants in Different Etiological Subtypes of Alzheimer's Disease. *Proc. Natl. Acad. Sci.* **2017**, *114* (49), 13018–13023. <https://doi.org/10.1073/pnas.1713215114>.
- (14) Condello, C.; Lemmin, T.; Stöhr, J.; Nick, M.; Wu, Y.; Maxwell, A. M.; Watts, J. C.; Caro, C. D.; Oehler, A.; Keene, C. D.; Bird, T. D.; Duinen, S. G. van; Lannfelt, L.; Ingelsson, M.; Graff, C.; Giles, K.; DeGrado, W. F.; Prusiner, S. B. Structural Heterogeneity and Intersubject Variability of A β in Familial and Sporadic Alzheimer's Disease. *Proc. Natl. Acad. Sci.* **2018**, 201714966. <https://doi.org/10.1073/pnas.1714966115>.
- (15) Condello, C.; Stöehr, J. A β Propagation and Strains: Implications for the Phenotypic Diversity in Alzheimer's Disease. *Neurobiol. Dis.* **2018**, *109* (Pt B), 191–200. <https://doi.org/10.1016/j.nbd.2017.03.014>.
- (16) Colletier, J.-P.; Laganowsky, A.; Landau, M.; Zhao, M.; Soriaga, A. B.; Goldschmidt, L.; Flot, D.; Cascio, D.; Sawaya, M. R.; Eisenberg, D. Molecular Basis for Amyloid- β Polymorphism. *Proc. Natl. Acad. Sci.* **2011**, *108* (41), 16938–16943. <https://doi.org/10.1073/pnas.1112600108>.
- (17) Toyama, B. H.; Weissman, J. S. Amyloid Structure: Conformational Diversity and Consequences. *Annu. Rev. Biochem.* **2011**, *80*. <https://doi.org/10.1146/annurev-biochem-090908-120656>.
- (18) Cohen, M. L.; Kim, C.; Haldiman, T.; ElHag, M.; Mehndiratta, P.; Pichet, T.; Lissemore, F.; Shea, M.; Cohen, Y.; Chen, W.; Blevins, J.; Appleby, B. S.; Surewicz, K.; Surewicz, W. K.;

- Sajatovic, M.; Tatsuoka, C.; Zhang, S.; Mayo, P.; Butkiewicz, M.; Haines, J. L.; Lerner, A. J.; Safar, J. G. Rapidly Progressive Alzheimer's Disease Features Distinct Structures of Amyloid- β . *Brain* **2015**, *138* (4), 1009–1022. <https://doi.org/10.1093/brain/awv006>.
- (19) Qiang, W.; Yau, W.-M.; Lu, J.-X.; Collinge, J.; Tycko, R. Structural Variation in Amyloid- β Fibrils from Alzheimer's Disease Clinical Subtypes. *Nature* **2017**, *541* (7636), 217–221. <https://doi.org/10.1038/nature20814>.
- (20) Watts, J. C.; Condello, C.; Stöhr, J.; Oehler, A.; Lee, J.; DeArmond, S. J.; Lannfelt, L.; Ingelsson, M.; Giles, K.; Prusiner, S. B. Serial Propagation of Distinct Strains of A β Prions from Alzheimer's Disease Patients. *Proc. Natl. Acad. Sci.* **2014**, *111* (28), 10323–10328. <https://doi.org/10.1073/pnas.1408900111>.
- (21) Stohr, J.; Watts, J. C.; Mensinger, Z. L.; Oehler, A.; Grillo, S. K.; DeArmond, S. J.; Prusiner, S. B.; Giles, K. Purified and Synthetic Alzheimer's Amyloid Beta (A β) Prions. *Proc. Natl. Acad. Sci.* **2012**, *109* (27), 11025–11030. <https://doi.org/10.1073/pnas.1206555109>.
- (22) Stohr, J.; Condello, C.; Watts, J. C.; Bloch, L.; Oehler, A.; Nick, M.; DeArmond, S. J.; Giles, K.; DeGrado, W. F.; Prusiner, S. B. Distinct Synthetic AB Prion Strains Producing Different Amyloid Deposits in Bigenic Mice. *Proc. Natl. Acad. Sci.* **2014**, *111* (28), 10329–10334. <https://doi.org/10.1073/pnas.1408968111>.
- (23) Bateman, R. J.; Aisen, P. S.; De Strooper, B.; Fox, N. C.; Lemere, C. A.; Ringman, J. M.; Salloway, S.; Sperling, R. A.; Windisch, M.; Xiong, C. Autosomal-Dominant Alzheimer's Disease: A Review and Proposal for the Prevention of Alzheimer's Disease. *Alzheimers Res. Ther.* **2011**, *3* (1), 1. <https://doi.org/10.1186/alzrt59>.

- (24) Korenberg, J. R.; Pulst, S.-M.; Neve, R. L.; West, R. The Alzheimer Amyloid Precursor Protein Maps to Human Chromosome 21 Bands Q21.105–Q21.05. *Genomics* **1989**, *5* (1), 124–127. [https://doi.org/10.1016/0888-7543\(89\)90095-5](https://doi.org/10.1016/0888-7543(89)90095-5).
- (25) Mann, D. M. A.; Esiri, M. M. The Pattern of Acquisition of Plaques and Tangles in the Brains of Patients under 50 Years of Age with Down’s Syndrome. *J. Neurol. Sci.* **1989**, *89* (2), 169–179. [https://doi.org/10.1016/0022-510X\(89\)90019-1](https://doi.org/10.1016/0022-510X(89)90019-1).
- (26) Castro, P.; Zaman, S.; Holland, A. Alzheimer’s Disease in People with Down’s Syndrome: The Prospects for and the Challenges of Developing Preventative Treatments. *J. Neurol.* **2017**, *264* (4), 804–813. <https://doi.org/10.1007/s00415-016-8308-8>.
- (27) Hof, P. R.; Bouras, C.; Perl, D. P.; Sparks, D. L.; Mehta, N.; Morrison, J. H. Age-Related Distribution of Neuropathologic Changes in the Cerebral Cortex of Patients With Down’s Syndrome: Quantitative Regional Analysis and Comparison With Alzheimer’s Disease. *Arch. Neurol.* **1995**, *52* (4), 379–391. <https://doi.org/10.1001/archneur.1995.00540280065020>.
- (28) Davidson, Y. S.; Robinson, A.; Prasher, V. P.; Mann, D. M. A. The Age of Onset and Evolution of Braak Tangle Stage and Thal Amyloid Pathology of Alzheimer’s Disease in Individuals with Down Syndrome. *Acta Neuropathol. Commun.* **2018**, *6*. <https://doi.org/10.1186/s40478-018-0559-4>.
- (29) Ballard, C.; Mobley, W.; Hardy, J.; Williams, G.; Corbett, A. Dementia in Down’s Syndrome. *Lancet Neurol.* **2016**, *15* (6), 622–636. [https://doi.org/10.1016/S1474-4422\(16\)00063-6](https://doi.org/10.1016/S1474-4422(16)00063-6).
- (30) Fortea, J.; Vilaplana, E.; Carmona-Iragui, M.; Benejam, B.; Videla, L.; Barroeta, I.; Fernández, S.; Altuna, M.; Pegueroles, J.; Montal, V.; Valldeneu, S.; Giménez, S.;

- González-Ortiz, S.; Muñoz, L.; Estellés, T.; Illán-Gala, I.; Belbin, O.; Camacho, V.; Wilson, L. R.; Annus, T.; Osorio, R. S.; Videla, S.; Lehmann, S.; Holland, A. J.; Alcolea, D.; Clarimón, J.; Zaman, S. H.; Blesa, R.; Lleó, A. Clinical and Biomarker Changes of Alzheimer's Disease in Adults with Down Syndrome: A Cross-Sectional Study. *The Lancet* **2020**, *395* (10242), 1988–1997. [https://doi.org/10.1016/S0140-6736\(20\)30689-9](https://doi.org/10.1016/S0140-6736(20)30689-9).
- (31) Lott, I. T.; Head, E. Dementia in Down Syndrome: Unique Insights for Alzheimer Disease Research. *Nat. Rev. Neurol.* **2019**, *15* (3), 135–147. <https://doi.org/10.1038/s41582-018-0132-6>.
- (32) Snyder, H. M.; Bain, L. J.; Brickman, A. M.; Carrillo, M. C.; Esbensen, A. J.; Espinosa, J. M.; Fernandez, F.; Fortea, J.; Hartley, S. L.; Head, E.; Hendrix, J.; Kishnani, P. S.; Lai, F.; Lao, P.; Lemere, C.; Mobley, W.; Mufson, E. J.; Potter, H.; Zaman, S. H.; Granholm, A.-C.; Rosas, H. D.; Strydom, A.; Whitten, M. S.; Rafii, M. S. Further Understanding the Connection between Alzheimer's Disease and Down Syndrome. *Alzheimers Dement.* **2020**, *16* (7), 1065–1077. <https://doi.org/10.1002/alz.12112>.
- (33) Abrahamson, E. E.; Head, E.; Lott, I. T.; Handen, B. L.; Mufson, E. J.; Christian, B. T.; Klunk, W. E.; Ikonovic, M. D. Neuropathological Correlates of Amyloid PET Imaging in Down Syndrome. *Dev. Neurobiol.* **2019**, *79* (7), 750–766. <https://doi.org/10.1002/dneu.22713>.
- (34) Scholl, M.; Wall, A.; Thordardottir, S.; Ferreira, D.; Bogdanovic, N.; Langstrom, B.; Almkvist, O.; Graff, C.; Nordberg, A. Low PiB PET Retention in Presence of Pathologic CSF Biomarkers in Arctic APP Mutation Carriers. *Neurology* **2012**, *79* (3), 229–236. <https://doi.org/10.1212/WNL.0b013e31825fdf18>.

- (35) Rosen, R. F.; Ciliax, B. J.; Wingo, T. S.; Gearing, M.; Dooyema, J.; Lah, J. J.; Ghiso, J. A.; LeVine, H.; Walker, L. C. Deficient High-Affinity Binding of Pittsburgh Compound B in a Case of Alzheimer's Disease. *Acta Neuropathol. (Berl.)* **2010**, *119* (2), 221–233.
<https://doi.org/10.1007/s00401-009-0583-3>.
- (36) Matveev, S. V.; Spielmann, H. P.; Metts, B. M.; Chen, J.; Onono, F.; Zhu, H.; Scheff, S. W.; Walker, L. C.; LeVine, H. A Distinct Subfraction of A β Is Responsible for the High-Affinity Pittsburgh Compound B-Binding Site in Alzheimer's Disease Brain. *J. Neurochem.* **2014**, *131* (3), 356–368. <https://doi.org/10.1111/jnc.12815>.
- (37) Frid, P.; Anisimov, S. V.; Popovic, N. Congo Red and Protein Aggregation in Neurodegenerative Diseases. *Brain Res. Rev.* **2007**, *53* (1), 135–160.
<https://doi.org/10.1016/j.brainresrev.2006.08.001>.
- (38) Vassar, P. S.; Culling, C. F. Fluorescent Stains, with Special Reference to Amyloid and Connective Tissues. *Arch. Pathol.* **1959**, *68*, 487–498.
- (39) Jun, Y. W.; Cho, S. W.; Jung, J.; Huh, Y.; Kim, Y.; Kim, D.; Ahn, K. H. Frontiers in Probing Alzheimer's Disease Biomarkers with Fluorescent Small Molecules. *ACS Cent. Sci.* **2019**, *5* (2), 209–217. <https://doi.org/10.1021/acscentsci.8b00951>.
- (40) Stöhr, J.; Wu, H.; Nick, M.; Wu, Y.; Bhate, M.; Condello, C.; Johnson, N.; Rodgers, J.; Lemmin, T.; Acharya, S.; Becker, J.; Robinson, K.; Kelly, M. J. S.; Gai, F.; Stubbs, G.; Prusiner, S. B.; DeGrado, W. F. A 31-Residue Peptide Induces Aggregation of Tau's Microtubule-Binding Region in Cells. *Nat. Chem.* **2017**, *9* (9), 874–881.
<https://doi.org/10.1038/nchem.2754>.

- (41) Belloy, M. E.; Napolioni, V.; Greicius, M. D. A Quarter Century of APOE and Alzheimer's Disease: Progress to Date and the Path Forward. *Neuron* **2019**, *101* (5), 820–838.
<https://doi.org/10.1016/j.neuron.2019.01.056>.
- (42) Prasher, V. P.; Sajith, S. G.; Rees, S. D.; Patel, A.; Tewari, S.; Schupf, N.; Zigman, W. B. Significant Effect of APOE Epsilon 4 Genotype on the Risk of Dementia in Alzheimer's Disease and Mortality in Persons with Down Syndrome. *Int. J. Geriatr. Psychiatry* **2008**, *23* (11), 1134–1140. <https://doi.org/10.1002/gps.2039>.
- (43) Mayeux, R.; Stern, Y.; Ottman, R.; Tatemichi, T. K.; Tang, M. X.; Maestre, G.; Ngai, C.; Tycko, B.; Ginsberg, H. The Apolipoprotein Epsilon 4 Allele in Patients with Alzheimer's Disease. *Ann. Neurol.* **1993**, *34* (5), 752–754. <https://doi.org/10.1002/ana.410340527>.
- (44) Ossenkoppele, R.; Smith, R.; Mattsson-Carlgen, N.; Groot, C.; Leuzy, A.; Strandberg, O.; Palmqvist, S.; Olsson, T.; Jögi, J.; Stormrud, E.; Cho, H.; Ryu, Y. H.; Choi, J. Y.; Boxer, A. L.; Gorno-Tempini, M. L.; Miller, B. L.; Soleimani-Meigooni, D.; Iaccarino, L.; La Joie, R.; Baker, S.; Borroni, E.; Klein, G.; Pontecorvo, M. J.; Devous, M. D.; Jagust, W. J.; Lyoo, C. H.; Rabinovici, G. D.; Hansson, O. Accuracy of Tau Positron Emission Tomography as a Prognostic Marker in Preclinical and Prodromal Alzheimer Disease: A Head-to-Head Comparison Against Amyloid Positron Emission Tomography and Magnetic Resonance Imaging. *JAMA Neurol.* **2021**. <https://doi.org/10.1001/jamaneurol.2021.1858>.
- (45) Bennett, D. A.; Schneider, J. A.; Wilson, R. S.; Bienias, J. L.; Arnold, S. E. Neurofibrillary Tangles Mediate the Association of Amyloid Load With Clinical Alzheimer Disease and Level of Cognitive Function. *Arch. Neurol.* **2004**, *61* (3), 378–384.
<https://doi.org/10.1001/archneur.61.3.378>.

- (46) Aoyagi, A.; Condello, C.; Stöhr, J.; Yue, W.; Rivera, B. M.; Lee, J. C.; Woerman, A. L.; Halliday, G.; Duinen, S. van; Ingelsson, M.; Lannfelt, L.; Graff, C.; Bird, T. D.; Keene, C. D.; Seeley, W. W.; DeGrado, W. F.; Prusiner, S. B. A β and Tau Prion-like Activities Decline with Longevity in the Alzheimer's Disease Human Brain. *Sci. Transl. Med.* **2019**, *11* (490). <https://doi.org/10.1126/scitranslmed.aat8462>.
- (47) Leverenz, J. B.; Raskind, M. A. Early Amyloid Deposition in the Medial Temporal Lobe of Young Down Syndrome Patients: A Regional Quantitative Analysis. *Exp. Neurol.* **1998**, *150* (2), 296–304. <https://doi.org/10.1006/exnr.1997.6777>.
- (48) Lemere, C. A.; Blusztajn, J. K.; Yamaguchi, H.; Wisniewski, T.; Saido, T. C.; Selkoe, D. J. Sequence of Deposition of Heterogeneous Amyloid β -Peptides and APO E in Down Syndrome: Implications for Initial Events in Amyloid Plaque Formation. *Neurobiol. Dis.* **1996**, *3* (1), 16–32.
- (49) Iwatsubo, T.; Mann, D. M. A.; Odaka, A.; Suzuki, N.; Ihara, Y. Amyloid β Protein (A β) Deposition: A β 42(43) Precedes A β 40 in down Syndrome. *Ann. Neurol.* **1995**, *37* (3), 294–299. <https://doi.org/10.1002/ana.410370305>.
- (50) Wesseling, H.; Mair, W.; Kumar, M.; Schlaffner, C. N.; Tang, S.; Beerepoot, P.; Fatou, B.; Guise, A. J.; Cheng, L.; Takeda, S.; Muntel, J.; Rotunno, M. S.; Dujardin, S.; Davies, P.; Kosik, K. S.; Miller, B. L.; Berretta, S.; Hedreen, J. C.; Grinberg, L. T.; Seeley, W. W.; Hyman, B. T.; Steen, H.; Steen, J. A. Tau PTM Profiles Identify Patient Heterogeneity and Stages of Alzheimer's Disease. *Cell* **2020**, *183* (6), 1699-1713.e13. <https://doi.org/10.1016/j.cell.2020.10.029>.

- (51) Wisniewski, K. E.; Wisniewski, H. M.; Wen, G. Y. Occurrence of Neuropathological Changes and Dementia of Alzheimer's Disease in Down's Syndrome. *Ann. Neurol.* **1985**, *17* (3), 278–282. <https://doi.org/10.1002/ana.410170310>.
- (52) Braak, H.; Braak, E. Neuropathological Stageing of Alzheimer-Related Changes. *Acta Neuropathol. (Berl.)* **1991**, *82* (4), 239–259. <https://doi.org/10.1007/BF00308809>.
- (53) van Dyck, C. H. Anti-Amyloid- β Monoclonal Antibodies for Alzheimer's Disease: Pitfalls and Promise. *Biol. Psychiatry* **2018**, *83* (4), 311–319. <https://doi.org/10.1016/j.biopsych.2017.08.010>.
- (54) Armstrong, R. A. The Molecular Biology of Senile Plaques and Neurofibrillary Tangles in Alzheimer's Disease. *Folia Neuropathol.* **2009**, *47* (4), 289–299.
- (55) Harada, R.; Okamura, N.; Furumoto, S.; Yoshikawa, T.; Arai, H.; Yanai, K.; Kudo, Y. Use of a Benzimidazole Derivative BF-188 in Fluorescence Multispectral Imaging for Selective Visualization of Tau Protein Fibrils in the Alzheimer's Disease Brain. *Mol. Imaging Biol.* **2014**, *16* (1), 19–27. <https://doi.org/10.1007/s11307-013-0667-2>.
- (56) Simon, R. A.; Shirani, H.; Åslund, K. O. A.; Bäck, M.; Haroutunian, V.; Gandy, S.; Nilsson, K. P. R. Pentameric Thiophene-Based Ligands That Spectrally Discriminate Amyloid- β and Tau Aggregates Display Distinct Solvatochromism and Viscosity-Induced Spectral Shifts. *Chem. - Eur. J.* **2014**, *20* (39), 12537–12543. <https://doi.org/10.1002/chem.201402890>.
- (57) Condello, C.; Yuan, P.; Schain, A.; Grutzendler, J. Microglia Constitute a Barrier That Prevents Neurotoxic Protofibrillar A β 42 Hotspots around Plaques. *Nat. Commun.* **2015**, *6*, 6176. <https://doi.org/10.1038/ncomms7176>.
- (58) Ulrich, J. D.; Ulland, T. K.; Mahan, T. E.; Nyström, S.; Nilsson, K. P.; Song, W. M.; Zhou, Y.; Reinartz, M.; Choi, S.; Jiang, H.; Stewart, F. R.; Anderson, E.; Wang, Y.; Colonna, M.;

- Holtzman, D. M. ApoE Facilitates the Microglial Response to Amyloid Plaque Pathology. *J. Exp. Med.* **2018**, *215* (4), 1047–1058. <https://doi.org/10.1084/jem.20171265>.
- (59) Yuan, P.; Condello, C.; Keene, C. D.; Wang, Y.; Bird, T. D.; Paul, S. M.; Luo, W.; Colonna, M.; Baddeley, D.; Grutzendler, J. TREM2 Haplodeficiency in Mice and Humans Impairs the Microglia Barrier Function Leading to Decreased Amyloid Compaction and Severe Axonal Dystrophy. *Neuron* **2016**, *90* (4), 724–739. <https://doi.org/10.1016/j.neuron.2016.05.003>.
- (60) Xue, Q.-S.; Streit, W. J. Microglial Pathology in Down Syndrome. *Acta Neuropathol. (Berl.)* **2011**, *122* (4), 455–466. <https://doi.org/10.1007/s00401-011-0864-5>.
- (61) Martini, A. C.; Helman, A. M.; McCarty, K. L.; Lott, I. T.; Doran, E.; Schmitt, F. A.; Head, E. Distribution of Microglial Phenotypes as a Function of Age and Alzheimer’s Disease Neuropathology in the Brains of People with Down Syndrome. *Alzheimers Dement. Amst. Neth.* **2020**, *12* (1), e121113. <https://doi.org/10.1002/dad2.12113>.
- (62) Ovchinnikov, D. A.; Korn, O.; Virshup, I.; Wells, C. A.; Wolvetang, E. J. The Impact of APP on Alzheimer-like Pathogenesis and Gene Expression in Down Syndrome iPSC-Derived Neurons. *Stem Cell Rep.* **2018**, *11* (1), 32–42. <https://doi.org/10.1016/j.stemcr.2018.05.004>.
- (63) Doran, E.; Keator, D.; Head, E.; Phelan, M. J.; Kim, R.; Totoiu, M.; Barrio, J. R.; Small, G. W.; Potkin, S. G.; Lott, I. T. Down Syndrome, Partial Trisomy 21, and Absence of Alzheimer’s Disease: The Role of APP. *J. Alzheimers Dis.* **2017**, *56* (2), 459–470. <https://doi.org/10.3233/JAD-160836>.
- (64) Wiseman, F. K.; Pulford, L. J.; Barkus, C.; Liao, F.; Portelius, E.; Webb, R.; Chávez-Gutiérrez, L.; Cleverley, K.; Noy, S.; Sheppard, O.; Collins, T.; Powell, C.; Sarell, C. J.;

- Rickman, M.; Choong, X.; Tosh, J. L.; Siganporia, C.; Whittaker, H. T.; Stewart, F.; Szaruga, M.; Murphy, M. P.; Blennow, K.; de Strooper, B.; Zetterberg, H.; Bannerman, D.; Holtzman, D. M.; Tybulewicz, V. L. J.; Fisher, E. M. C. Trisomy of Human Chromosome 21 Enhances Amyloid- β Deposition Independently of an Extra Copy of APP. *Brain* **2018**, *141* (8), 2457–2474. <https://doi.org/10.1093/brain/awy159>.
- (65) Ryoo, S.-R.; Jeong, H. K.; Radnaabazar, C.; Yoo, J.-J.; Cho, H.-J.; Lee, H.-W.; Kim, I.-S.; Cheon, Y.-H.; Ahn, Y. S.; Chung, S.-H.; Song, W.-J. DYRK1A-Mediated Hyperphosphorylation of Tau. *J. Biol. Chem.* **2007**, *282* (48), 34850–34857. <https://doi.org/10.1074/jbc.M707358200>.
- (66) Wegiel, J.; Dowjat, K.; Kaczmarek, W.; Kuchna, I.; Nowicki, K.; Frackowiak, J.; Mazur Koleccka, B.; Wegiel, J.; Silverman, W. P.; Reisberg, B.; deLeon, M.; Wisniewski, T.; Gong, C.-X.; Liu, F.; Adayev, T.; Chen-Hwang, M.-C.; Hwang, Y.-W. The Role of Overexpressed DYRK1A Protein in the Early Onset of Neurofibrillary Degeneration in Down Syndrome. *Acta Neuropathol. (Berl.)* **2008**, *116* (4), 391–407. <https://doi.org/10.1007/s00401-008-0419-6>.
- (67) Song, W.-J.; Song, E.-A. C.; Choi, S.-H.; Baik, H.-H.; Jin, B. K.; Kim, J. H.; Chung, S.-H. Dyrk1A-Mediated Phosphorylation of RCAN1 Promotes the Formation of Insoluble RCAN1 Aggregates. *Neurosci. Lett.* **2013**, *554*, 135–140. <https://doi.org/10.1016/j.neulet.2013.08.066>.
- (68) Giles, K.; Berry, D. B.; Condello, C.; Hawley, R. C.; Gallardo-Godoy, A.; Bryant, C.; Oehler, A.; Elepano, M.; Bhardwaj, S.; Patel, S.; Silber, B. M.; Guan, S.; DeArmond, S. J.; Renslo, A. R.; Prusiner, S. B. Different 2-Aminothiazole Therapeutics Produce Distinct

- Patterns of Scrapie Prion Neuropathology in Mouse Brains. *J. Pharmacol. Exp. Ther.* **2015**, 355 (1), 2–12. <https://doi.org/10.1124/jpet.115.224659>.
- (69) Berry, D. B.; Lu, D.; Geva, M.; Watts, J. C.; Bhardwaj, S.; Oehler, A.; Renslo, A. R.; DeArmond, S. J.; Prusiner, S. B.; Giles, K. Drug Resistance Confounding Prion Therapeutics. *Proc. Natl. Acad. Sci.* **2013**, 110 (44), E4160–E4169. <https://doi.org/10.1073/pnas.1317164110>.
- (70) Selkoe, D. J. Alzheimer Disease and Aducanumab: Adjusting Our Approach. *Nat. Rev. Neurol.* **2019**, 15 (7), 365–366. <https://doi.org/10.1038/s41582-019-0205-1>.
- (71) Armstrong, R. A.; Smith, C. U. M. β -Amyloid (β /A4) Deposition in the Medial Temporal Lobe in Down's Syndrome: Effects of Brain Region and Patient Age. *Neurobiol. Dis.* **1994**, 1 (3), 139–144. <https://doi.org/10.1006/nbdi.1994.0017>.
- (72) Annus, T.; Wilson, L. R.; Hong, Y. T.; Acosta–Cabronero, J.; Fryer, T. D.; Cardenas–Blanco, A.; Smith, R.; Boros, I.; Coles, J. P.; Aigbirhio, F. I.; Menon, D. K.; Zaman, S. H.; Nestor, P. J.; Holland, A. J. The Pattern of Amyloid Accumulation in the Brains of Adults with Down Syndrome. *Alzheimers Dement.* **2016**, 12 (5), 538–545. <https://doi.org/10.1016/j.jalz.2015.07.490>.
- (73) Zhong, L.; Xie, Y.-Z.; Cao, T.-T.; Wang, Z.; Wang, T.; Li, X.; Shen, R.-C.; Xu, H.; Bu, G.; Chen, X.-F. A Rapid and Cost-Effective Method for Genotyping Apolipoprotein E Gene Polymorphism. *Mol. Neurodegener.* **2016**, 11 (1), 2. <https://doi.org/10.1186/s13024-016-0069-4>.
- (74) *MATLAB*; The MathWorks Inc.: Natick, Massachusetts, 2021.

APPENDIX A

Chapter 1 supplementary information

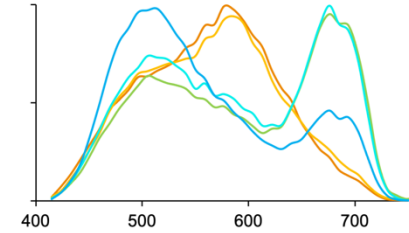
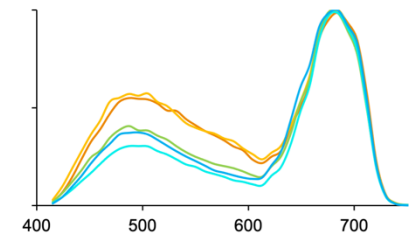
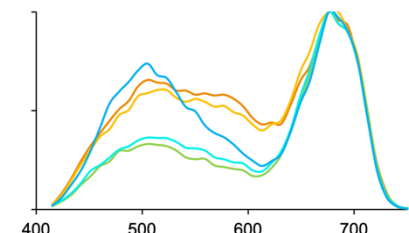
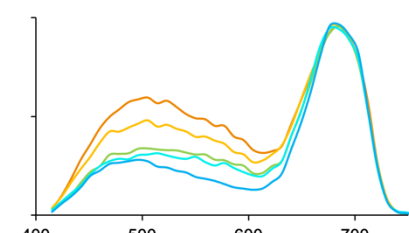
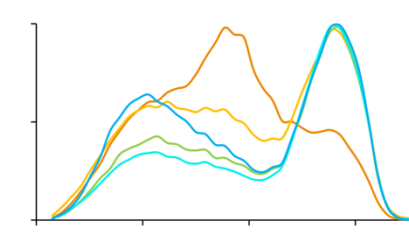
Table A.1. Spectral properties of dyes tested for conformation sensitivity. Dyes at various concentrations were used to stain A β aggregates suspended in 1% agarose gel or R3 “tiny” tau aggregates suspended in PBS. In most cases, multiple excitation wavelengths were tested, with the optimal wavelength listed below. The following additional dyes were tested without yielding sufficient fluorescence to determine an emission spectrum: THK-111, K114, thiazine red, resorufin red, congo red, and CRANAD-2. When a range of emission wavelengths is given, the peak emission spectra were different across experiments.

Dye	Excitation (nm)	Peak emission (A β 40) (nm)	Peak emission (A β 42) (nm)	Peak emission (R3 tau) (nm)
BAP-1	594	650	641	665
BSB	405	-	-	485-510
BF-188	405	586	523	530
CRANAD-3	561	628	619	690
FSB	405	499	526	465-510
NIAD-4	492	-	-	620
Nile red	561	624	615	615
PBB5	633	685	685	690
THK-265	594	636	627	-
THK-523	440	-	-	470
ThT	405	481	481	480

Table A.2. Spectral changes of BF-188 /PBB5-stained A β fibrils compared to procedural elements. Fibrils comprised of A β 40 and A β 42 peptide mixtures were prepared in two batches, designated “A” and “B”, and embedded in agarose gel in a microplate. Dye solution (5 μ M BF-188 + 5 μ M PBB5) was added to the wells; in some experiments, after 1 h the dye was washed out and replaced with PBS prior to imaging. The third and fourth columns respectively indicate the length of time between fibril plating and staining and between staining and imaging. Whether or not the specific wells shown had been previously imaged is also indicated. The charts show the peak-normalized average fluorescence intensity of the fibrils as a function of wavelength.

Fibril prep	Dye wash-out	Time to staining	Time to imaging	Prev. imaged	Laser power (%)	Spectra				
						A β 42	3:1	1:1	1:3	A β 40
A	yes	1 d	4 h	no	40					
A	yes	5 d	4 h	no	20					
A	yes	1 w	4 h	no	40					
A	yes	1 w	4 h	no	40					
B	yes	1 d	4 h	yes	80					

Fibril prep	Dye wash-out	Time to staining	Time to imaging	Prev. imaged	Laser power (%)	Spectra				
						A β 42	3:1	1:1	1:3	A β 40
B	yes	2 d	1 d	no	85					
B	yes	3 w	4 h	no	80					
B	yes	3 w	4 h	no	80					
B	yes	3 w	1 d	yes	80					
B	yes	3.5 w	4 h	no	100					
B	no	1 d	1 d	no	40					

Fibril prep	Dye wash-out	Time to staining	Time to imaging	Prev. imaged	Laser power (%)	Spectra				
						A β 42	3:1	1:1	1:3	A β 40
B	no	3 d	3 d	yes	25					
B	no	2 w	2 w	yes	100					
B	no	2 w	1 d	yes	100					
B	no	4 h	1 h	no	50					
B	no	4 h	1 d	yes	100					

APPENDIX B

Chapter 2 supplementary information

In addition to the supplementary table and figures mentioned in Chapter 2, this appendix contains two pieces of work that were unable to be incorporated into the larger picture of AD in DS: (1) the prion-like activity of A β and tau isolated from human tissues and (2) the verification of DS through quantification of APP copy number. The results and discussion presented here are entirely preliminary, but are included to benefit future work in these areas.

B.1 METHODS

qPCR assay for APP copy number

An assay was designed and preliminarily tested to determine the copy number (CN) of the *APP* gene from an individual's genomic DNA. Primers and TaqMan probes were synthesized by Integrated DNA Technologies (Coralville, IA) and are listed in **Table B.1**. The ACTB oligos were designed by Zhong et al. (2016)¹. The APP probe was designed to span a central region of the human *APP* gene. APP primers were designed to encompass the APP probe and have similar melting temperatures as for ACTB. A reaction master mix was prepared containing 1X Taq ProAmp MM (Thermo Fisher #A30871) and 0.25 μ M of each ACTB and APP primer and probe. In the wells of a 384-well plate, 1.25 μ L DNA (15 ng/ μ L) was added to 10.75 μ L master mix so that each 20- μ L reaction contained 1 ng DNA and 0.25 μ M each primer and probe. After brief centrifugation to remove air bubbles, the plate was thermocycled in a Quant Studio 6 Flex real-

time PCR system equipped with Applied Biosystems software. The cycling conditions are outlined in **Table B.1**. DNA quantity was quantified through detection of the probe labels TAMRA (ex/em 555/580 nm) and HEX (538/554 nm), using ROX (575/602 nm) as a passive reference dye.

The number of copies of a gene in a PCR assay will determine the number of amplification cycles required to raise the amount of detectable material above a given signal threshold, or normalized reporter value (ΔR_n). Therefore, if a subject has three copies of APP (i.e. has DS), it will take 3/2 fewer amplification cycles to reach the same amount of bound APP-specific probe in a reaction well as for any gene of which the subject has two. Therefore, APP copy number was determined by first comparing the threshold cycle number (ΔC_T) of the reference gene ACTB to that of APP in DS and in AD according to the following equation:

$$\Delta\Delta C_T = (C_T^{[APP]} - C_T^{[ACTB]})_{DS} - (C_T^{[APP]} - C_T^{[ACTB]})_{AD} \quad (B.1)$$

By testing many non-DS samples, we can obtain a reliable average ΔC_T for AD to use in the second half of the equation. To get relative CN, we then calculate:

$$CN = 2^{-\Delta\Delta C_T} \quad (B.2)$$

A relative CN = 1.5 would mean precisely three copies of APP for every two copies of ACTB, indicating trisomy at least at this critical region of Chr21.

ACTB and APP probe efficiency was determined by serial diluting DNA from two AD subjects and comparing amplification to known DNA amount for each. By plotting the threshold cycle value against the dilution factor on a base-10 logarithmic plot, amplification efficiency E of each probe was calculated as:

$$E = 10 \times \frac{-1}{m} - 1 \quad (B.3)$$

where m is the slope of the linear fit. A slope of -3.32 indicates 100% probe efficiency, corresponding to the calculation of copy number using base 2 in **Equation B.2**.

Table B.1. Primers and conditions used in APP copy number assay.

Primer or step	Sequence or condition
ACTB Forward	5'-GACGTGGACATCCGCAAAGAC -3'
ACTB Reverse	5'-CAGGTCAGCTCAGGCAGGAA -3'
ACTB Probe	5'-HEX-TGCTGTCTGGCGGCACCACCATGTACC-BHQ1-3'
APP Forward	5'-CCTTCTCGTTCCTGACAAGTGC-3'
APP Reverse	5'-CACGGCACAGGCACATAATGAATC-3'
APP Probe	5'-TAMRA-CTCATCTTCACTGGCACACCGTC-GCCAAAGAGG-IBFQ-3'
Pre-read	60 °C for 30 s
Initial denaturation	95 °C for 10 min
Denaturation (x40 cycles)	95°C for 15 s
Annealing/Extension (x40)	64 °C for 60 s
Post-read	60 °C for 30 s

Preparation A β and tau PTA extracts

PTA precipitation was performed by incubating 10% (wt/vol) brain homogenate from frontal cortical tissue in 2% (vol/vol) sarkosyl and 0.5% (vol/vol) benzonase (Sigma) at 37 °C with constant agitation (1,200 rpm) in an orbital shaker for 2 h. Sodium phosphotungstic acid (PTA) was dissolved in double-distilled H₂O, and the pH was adjusted to 7.0. PTA was added to the solution to a final concentration of 2% (vol/vol), which was then incubated overnight in the same conditions. The sample was centrifuged at 16,000 \times g for 30 min at room temperature, and the supernatant was removed. The resulting pellet was resuspended in 2% (vol/vol) sarkosyl in PBS and 2% (vol/vol) PTA in double-distilled H₂O, pH 7.0. The sample was again incubated for at least 1 h before a second centrifugation. The supernatant was again removed, and the pellet was resuspended in PBS using 10% of the initial starting volume.

Cellular assay for quantifying prion-like activity of human A β and tau

PTA precipitates were assayed for prion-like activity using a cellular bioassay as previously described^{2,3}. Cells were plated in a 384-well plate at 3000 cells (70 μ L) per well with Hoechst 33342 (0.1 μ g/mL) (Thermo Fisher). PTA-precipitated protein was incubated with Lipofectamine 2000 (1.5% final volume) and OptiMEM (78.5% final volume) (both from Thermo Fisher) for 2 h at room temperature and added to the cells (10 μ L). Plates were incubated at 37 °C and imaged every 24 h on an IN Cell Analyzer (GE Healthcare) over 3 days. Using an overlay of the DAPI and FITC channels, aggregates in living cells were assessed from four regions in each of four replicate wells. Tau and α -synuclein infectivity data were validated in cells expressing proteins not tagged with YFP.

B.2 RESULTS & DISCUSSION

APP copy number can be determined in high throughput using qPCR

The utility and accuracy of the APP copy number assay was initially assessed by comparing DNA from five karyotype-confirmed DS subjects to that from three familial AD subjects (gifts from C. Condello). Using a threshold of 0.30 ΔR_n , we determined an average $\Delta\Delta C_T$ for AD subjects (two copies of APP) = 0.189, which allowed for the calculation of APP copy number in the DS subjects using **Equation B.1 (Table B.2)**. The expected relative CN was 1.5, indicating 3 copies of APP for every two of ACTB, but on average the DS subjects were found to have 1.33 ± 0.1 CN. Two important factors likely impacted this result: pipetting precision and the relative efficiencies of the amplification of the APP and ACTB probes. The former is not trivial in qPCR,

Table B.2. APP copy number analysis of five DS subjects. DNA from five DS and three AD subjects was amplified using a TaqMan qPCR assay. The signal from an APP-specific probe was compared to that from a probe for the housekeeping gene ACTB at an amplification signal threshold of 0.30. Relative CN was first calculated using an assumed 100% probe efficiency. A corrected relative CN was also calculated using the determined efficiencies of the APP probe as 1.896 and of the ACTB probe as 1.986. The expected relative copy number of APP in DS is 1.50, corresponding to 3 copies of the APP gene.

Subject	$\Delta\Delta C_T$	Relative CN	Corrected relative CN
DS-1	0.350	1.27	1.33
DS-2	0.339	1.27	1.42
DS-3	0.380	1.30	1.42
DS-4	0.590	1.50	1.68
DS-5	0.359	1.28	1.33

where the slightest errors are amplified to significance; in future assays, it is highly recommended that newly-calibrated pipettes are used and abundant care is taken to ensure precision.

To assess and accommodate the latter, however, we tested the amplification efficiencies of the two probes using a standard curve according to **Equation B.3**. The two tested AD subjects showed APP probe efficiencies of 1.814 and 1.978 (average = 1.896) and ACTB probe efficiencies of 1.964 and 2.008 (average = 1.986). Though more similar values would be expected between subjects, the aforementioned pipetting issue likely played a role, while at least a few more subjects should also be tested in order to increase the precision of the result. Regardless, these average efficiencies were used to correct the relative CNs in **Table B.2**. This correction improved the accuracy of the average DS CN to 1.44 ± 0.1 .

The approximate accuracy of the determined APP CN values in a very first test of the assay, we believe this assay is a promising avenue for confirming trisomy 21 (at least in the APP region of Chr21) from genomic DNA. A major benefit of the assay is the throughput: since ACTB and APP probes are analyzed in the same reaction well, with three replicates per subject, approximately

100 subjects could be analyzed simultaneously. With practice, from plate set-up to analysis, the entire assay could be completed within about 8 hours.

For the main body of our analysis of AD in DS, we ultimately determined that verifying the presence of three copies of APP in our DS subjects was not of paramount importance; the chances of DS mosaicism are less than 5% (ref. 4) and we had only vague hypotheses about the role of APP itself in affecting A β strain profiles (see **2.4 Discussion**). However, if this becomes compelling in future work, it should take minimal further optimization of the assay described here to accurately determine APP CN in hundreds of DS samples.

A β and tau prion-like activities varies among individuals but not by cohort

The ability of an amyloidogenic protein to propagate its structure by inducing the misfolding of other peptides through prion-like templating can be tested using a cellular bioassay. In the assay, HEK cells express the protein of interest fused to YFP and have minimal base-line fluorescence. When brain-derived protein material is added to the cell media, it can be taken up by the cells. If the protein has prion-like activity, it induces the aggregation of the expressed protein, resulting in aggregates of fluorescent YFP that can be measured by microscopy. We hypothesized that a subset of DS subjects, possibly with unique conformations of A β as determined by our fluorescent probe method, would have significantly different A β prion-like activities compared to other DS or AD subjects.

We tested PTA protein extracts (0.015x concentration) from our AD and DS subjects in cells expressing A β 40, A β 42, R3 tau, R4 tau (P301L/V337M), and K18 mutant tau (**Figure B.1**). As a negative control, we also tested the extracts in cells expressing mutant α -synuclein, which would not be present in any of our AD or DS subjects. On average across subjects, we detected

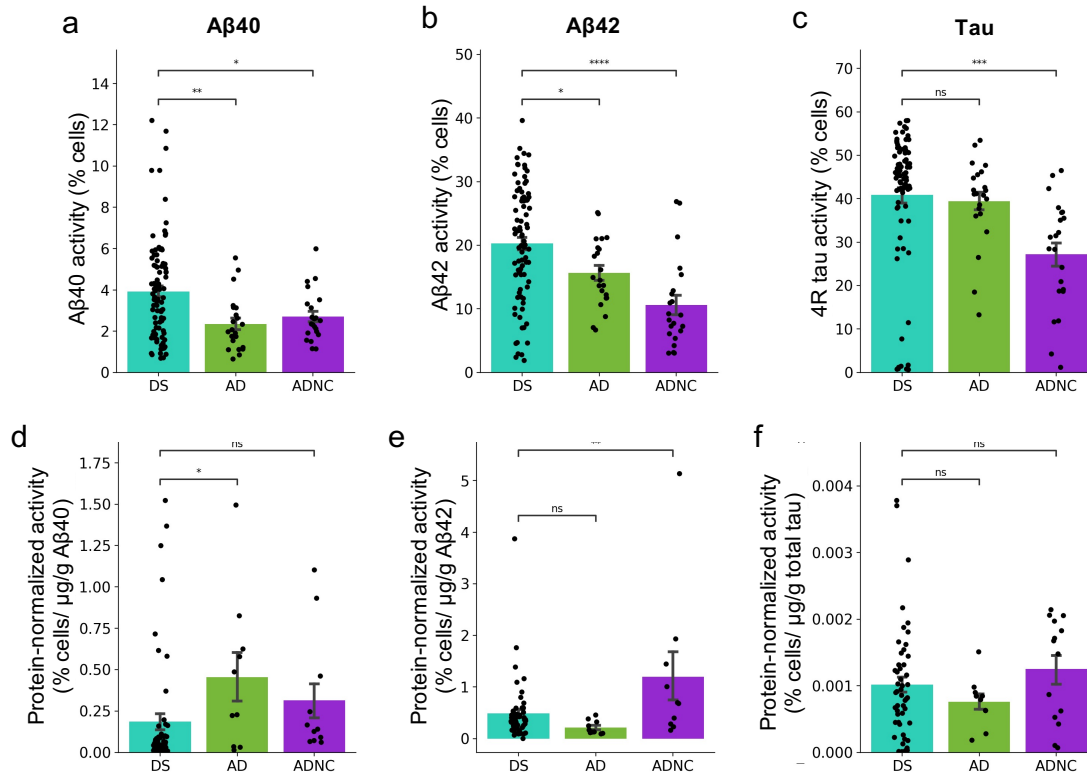


Figure B.1. Preliminary Aβ and tau prion-like activities in a cellular bioassay. PTA protein extracts from frontal cortical tissue were assayed for prion-like activity using a cellular bioassay that measures the aggregation of expressed Aβ40, Aβ42, or 4R mutant (P301L/V337M) tau fused to YFP due to templated misfolding. Activity was measured as the % of living cells that contained fluorescent protein aggregates. The activities shown in A-C were normalized in D-F to the total amount of the given protein normalized to total brain protein (see 2.2 Methods). Significance values were determined by student's two-tailed t-test. *: 0.01 < p ≤ 0.05; **: 0.001 < p ≤ 0.01, ***: 0.0001 < p ≤ 0.001, ****: p ≤ 0.0001. ns = not significant.

2.7 ± 2% cells with YFP-positive aggregates in α-synuclein-expressing cells, which was only marginally higher than when adding PBS to the cells (2.29 ± 0.02%). Surprisingly, however, Aβ40 activity was also low (Figure B.1A) compared to values previously observed in some sporadic AD subjects (data not shown) and compared to initial tests of the assay in DS subjects a few years prior. This possibly suggests a recent decrease in Aβ40 cell line robustness. Aβ42 activity was most significantly different among cohorts (Figure B.1B), but once normalized to per-subject Aβ42 concentrations (Figure B.1E), the difference between AD and DS vanished, while ADNC

cases appeared to have the highest activity. This follows the fact that ADNC cases had by far the lowest A β 42 concentrations, but indicates that the assay is ultimately likely not reporting prion-like templating behavior. Perhaps only subjects with substantial A β 42 loads should be compared to one another, to avoid biasing results towards those with nearly non-existent protein amounts. In the 4R tau assay (**Figure B.1C**), both AD and DS subjects tended to show activities that clustered between 40-60% cells with aggregates, which may indicate assay saturation. This assay should probably be repeated at higher dilution of PTA extract. We did not observe any significant trends in activity relative to patient age or A β strain profile in PCA (data not shown).

To attempt to improve A β 40 and R3 tau assay sensitivity, we repeated the assay at 0.03x PTA concentration (data not shown). However, the aggregation response did not significantly change. This suggests that A β 40 and R3 tau assay sensitivities may be due to an inability of the expressed peptides to be misfolded through templating. We suggest that the assays be optimized to ensure robust response to known prions before attempting to conclude differences among individuals in this study.

B.3 ADDITIONAL TABLE AND FIGURES

Table B.3. *APOE* primers and conditions used in PCR and sequencing.

Primer or Step	Sequence or Condition
PCR Forward	5'-AGCCCTTCTCCCCGCCTCCCCTGT-3'
PCR Reverse	5'-CTCCGCCACCTGCTCCTTCACCTCG-3'
Sequencing primer	GATGGACGAGACCATG
Initial denaturation	98 °C for 4 min
Denaturation (x35 cycles)	98 °C for 10 s
Annealing (x35)	68 °C for 30 s
Extension (x35)	72 °C for 45 s
Final extension	72 °C for 10 min

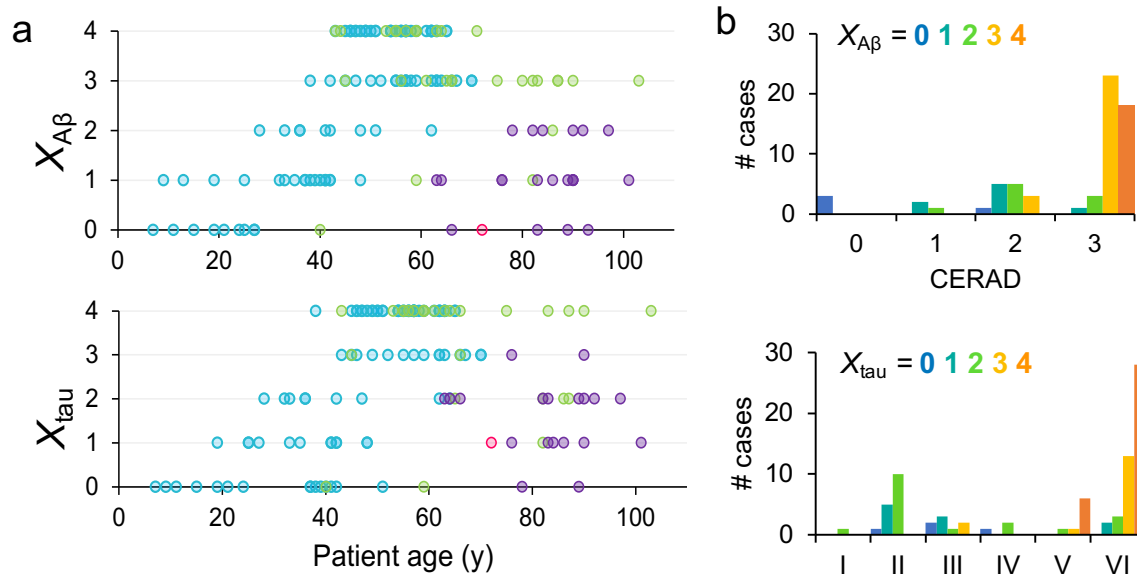


Figure B.2. A β and tau scores relative to patient age at death. (A) Scores were determined through manual evaluation of A β 40, A β 42, and pTau load in IHC-stained frontal cortical tissue sections. DS subjects are shown in blue, AD in green, ADNC in purple, and PT21 in pink. (B) Relationship between manual A β and tau scores and bank-provided scores determined at autopsy.

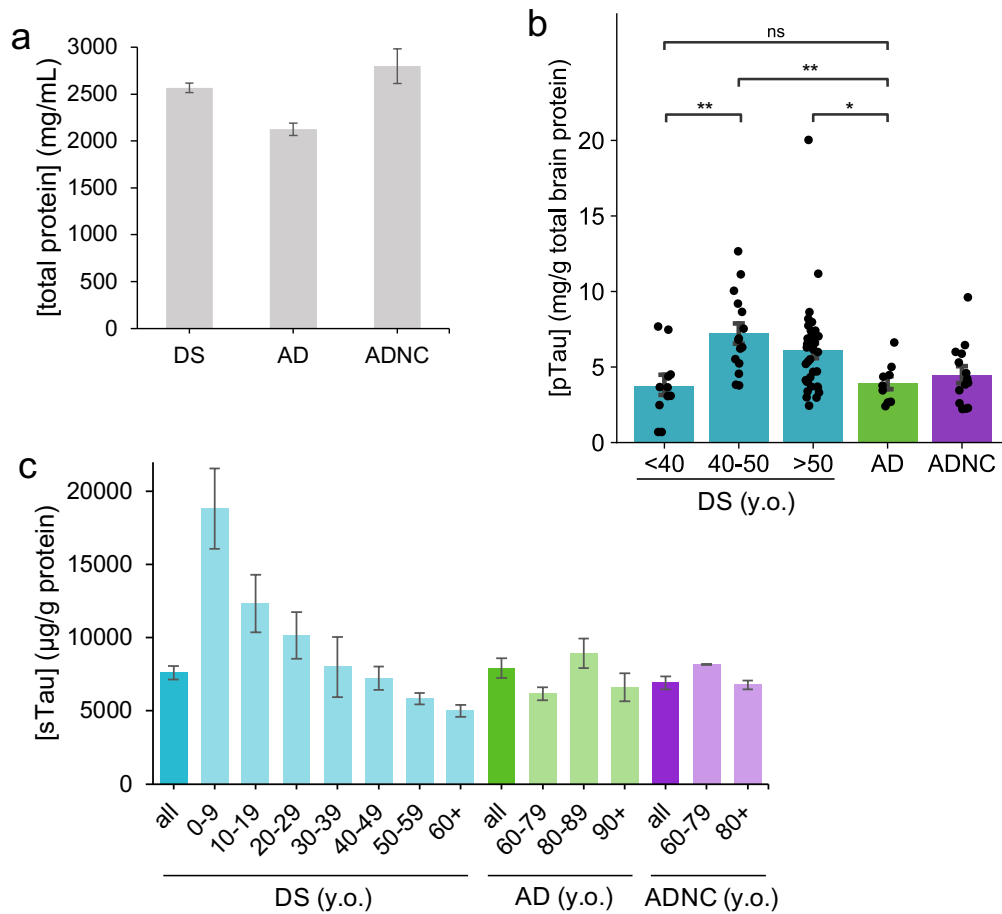


Figure B.3. Total protein and tau species concentrations in greater granularity. (A) Total protein in 10% BH assayed by BCA (B) S203/T205 pTau concentrations as measured by HTRF delineated by age in DS, \pm SEM. pTau is significantly higher in DS after 40 years of age compared to in younger DS individuals and compared to AD. p-value: *: $0.01 < p \leq 0.05$; **: $0.001 < p \leq 0.01$, ***: $0.0001 < p \leq 0.001$ (C) Soluble tau concentrations as measured by ELISA decline with age in DS, \pm SEM.

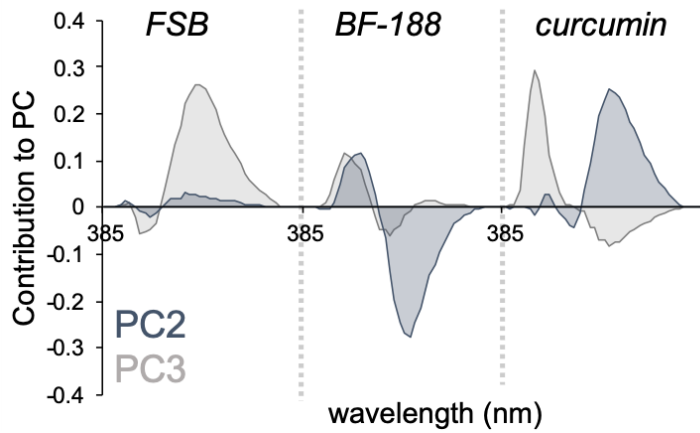


Figure B.4. Wavelength contributions to the principle component space. Each of the three conformation-sensitive dyes FSB, BF-188, and curcumin contribute to PC2 and PC3.

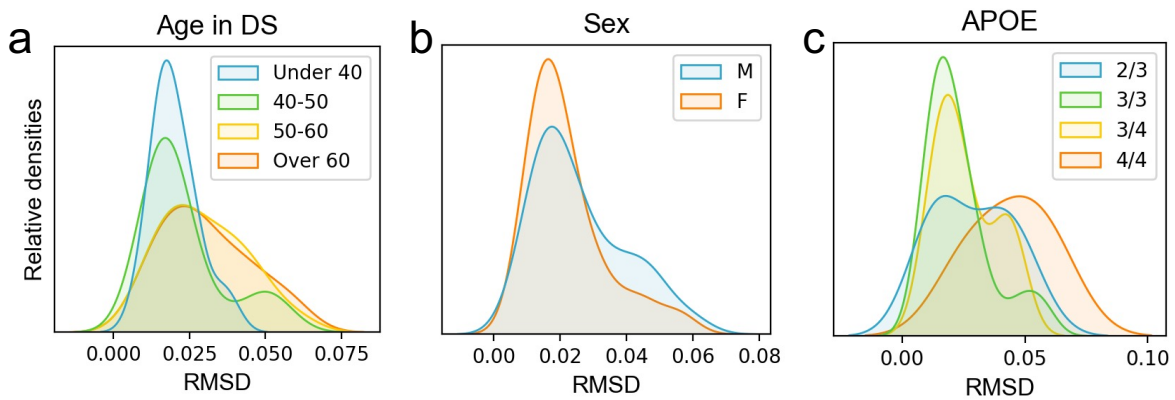


Figure B.5. Per-patient RMSD distributions by age, sex, and APOE. (A) RMSD by DS patient age at death, (B) by sex, and (C) by APOE genotype, when known. RMSD values were calculated as the distances in PC2, PC3, and PC4 of each vector from the centroid of all the vectors for a given case. The relative densities are shown as a Gaussian KDE, normalized to the area under the curve, of the RMSDs calculated for all the cases in a given group.

B.4 REFERENCES

- (1) Zhong, L.; Xie, Y.-Z.; Cao, T.-T.; Wang, Z.; Wang, T.; Li, X.; Shen, R.-C.; Xu, H.; Bu, G.; Chen, X.-F. A Rapid and Cost-Effective Method for Genotyping Apolipoprotein E Gene Polymorphism. *Mol. Neurodegener.* 2016, 11 (1), 2. <https://doi.org/10.1186/s13024-016-0069-4>.
- (2) Levine, D. J.; Stöhr, J.; Falese, L. E.; Ollesch, J.; Wille, H.; Prusiner, S. B.; Long, J. R. Mechanism of Scrapie Prion Precipitation with Phosphotungstate Anions. *ACS Chem. Biol.* 2015, 10 (5), 1269–1277. <https://doi.org/10.1021/cb5006239>.
- (3) Woerman, A. L.; Aoyagi, A.; Patel, S.; Kazmi, S. A.; Lobach, I.; Grinberg, L. T.; McKee, A. C.; Seeley, W. W.; Olson, S. H.; Prusiner, S. B. Tau Prions from Alzheimer’s Disease and Chronic Traumatic Encephalopathy Patients Propagate in Cultured Cells. *Proc. Natl. Acad. Sci. U. S. A.* 2016, 113 (50), E8187–E8196. <https://doi.org/10.1073/pnas.1616344113>.
- (4) Jackson-Cook, C. Constitutional and Acquired Autosomal Aneuploidy. *Clin. Lab. Med.* 2011, 31 (4), 481–vii. <https://doi.org/10.1016/j.cll.2011.08.002>.

APPENDIX C

Individual case characteristics

Table C.1. Biological data and experimental inclusion of each case. Case ID numbers, cohort, age, sex, and post-mortem interval (PMI) were provided by the tissue banks. *APOE* genotype was determined through Sanger sequencing of SNP-containing amplicons, which were generated from genomic DNA purified from frozen tissue. Neuropathological scores for A β ($X_{A\beta}$) and tau (X_{tau}) were assigned based on counting A β 42-, A β 40-, and pTau-positive lesions in one fixed frontal cortical tissue section stained using immunohistochemistry (IHC). The last four columns indicate whether the indicated experiment was attempted (“o”) or performed (“x”) on the case. For principal component analysis (PCA), an attempt (“o”) means that a tissue section was stained with BF-188, FSB, and curcumin but that fluorescent plaques could not be detected or analyzed for one or all of the dyes. Enzyme-linked immunosorbent assays (ELISAs) were used to measure APP and soluble tau concentrations. Homologous time-resolved fluorescence (HTRF) was used to measure A β and insoluble tau concentrations, including pTau. A cellular bioassay (CB) was used to measure the prion-like activity of A β and tau species. Bank abbreviations: UW = University of Washington; UMD = University of Maryland; MIA = University of Miami; BCN = IDIBAPS (Barcelona); MTS = Mt Sinai School of Medicine; HVD = Harvard University; MCR = University of Manchester; KCL = King’s College London; UCI = University of California, Irvine; NYU = New York University. A tick (-) indicates missing information. * = karyotype-confirmed DS.

Bank	ID	Cohort	Age	Sex	PMI (h)	<i>APOE</i>	$X_{A\beta}$	X_{tau}	IHC	PCA	ELISA	HTRF	CB
UW	12664	DS	48	F	3	3/3	-	-	-	-	x	-	x
UW	11-0033	DS	59	F	8	-	4	3	x	-	-	-	-
UW	11-1450	DS	49	M	14	-	4	4	x	-	-	-	-
UW	09-0007	DS	57	F	4	3/4	4	4	x	-	x	-	x
UW	00-0584	DS	62	F	4	3/3	4	4	x	-	x	-	x
UW	09-1549	DS	27	F	-	-	0	1	x	o	-	-	-
MIA	18_01	DS	24	M	24	3/3	0	0	x	o	x	-	x
MIA	19_01	DS	51	F	8	3/3	4	4	x	-	x	-	x
MIA	19_03	DS	57	M	11	3/4	4	4	x	-	x	-	x

Bank	ID	Cohort	Age	Sex	PMI (h)	APOE	X _{AB}	X _{tau}	IHC	PCA	ELISA	HTRF	CB
UMD	4273	DS	33	M	36	-	1	1	X	X	-	-	-
UMD	4335	DS*	28	M	26	4/4	2	2	X	X	X	X	X
UMD	5005	DS*	39	F	12	-	1	0	X	X	-	-	-
UMD	5277	DS*	19	M	26	3/4	1	1	X	X	X	X	X
UMD	5341	DS*	25	M	24	3/3	1	1	X	X	X	X	X
UMD	5713	DS	25	M	22	2/3	0	1	X	0	X	X	X
UMD	4530	DS*	47	F	7	3/4	4	4	X	X	X	X	X
UMD	4659	DS*	46	F	7	3/4	4	4	X	X	X	X	X
UMD	4785	DS*	55	F	25	3/3	3	3	X	X	X	X	X
UMD	4870	DS*	51	F	4	2/3	4	4	X	X	X	X	X
UMD	4904	DS*	40	M	10	3/3	1	0	X	0	X	X	X
UMD	5386	DS*	64	M	20	3/4	3	2	X	X	X	X	X
UMD	5510	DS*	65	M	10	3/3	4	4	X	X	X	X	X
UMD	5600	DS	57	F	6	3/3	3	4	X	X	X	X	X
UMD	5783	DS	41	M	15	3/4	1	1	X	X	X	X	X
UMD	6151	DS	57	M	5	3/3	4	4	X	X	X	X	X
UMD	2854	DS*	15	M	14	-	0	0	X	-	X	-	-
UMD	2135	DS*	2	M	12	-	-	-	X	-	X	-	-
UMD	1947	DS*	0	F	24	-	-	-	X	-	-	-	-
UMD	267	DS	0	M	28	-	-	-	X	-	-	-	-
UMD	570	DS	2	M	24	-	-	-	X	-	-	-	-
UMD	714	DS*	2	M	17	-	-	-	-	-	-	-	-
UMD	718	DS*	1	F	28	-	-	-	X	-	-	-	-
UMD	832	DS*	1	M	23	-	-	-	X	-	-	-	-
UMD	1267	DS	10	M	17	-	-	-	-	-	-	-	-
UMD	1276	DS*	13	M	25	-	-	-	-	-	-	-	-
UMD	1282	DS*	0	F	28	-	-	-	X	-	-	-	-
UMD	4204	DS	9	F	30	-	1	0	X	0	-	-	-

Bank	ID	Cohort	Age	Sex	PMI (h)	APOE	X _{Aβ}	X _{tau}	IHC	PCA	ELISA	HTRF	CB
UMD	5301	DS*	3	F	11	-	-	-	-	-	X	-	-
UMD	5874	ADNC	63	F	25	3/3	1	2	X	-	X	X	X
UMD	6054	ADNC	76	M	15	3/4	1	3	X	-	X	X	X
BCN	665	DS	59	F	8	3/4	3	4	X	X	X	X	X
BCN	714	DS	36	F	12	3/3	2	2	X	X	X	X	X
BCN	907	DS	63	M	6	3/3	3	4	X	X	X	X	X
BCN	1028	DS	67	F	11	3/3	3	3	X	X	X	X	X
BCN	1335	DS	62	F	9	3/4	4	4	X	X	X	X	X
BCN	1469	DS	62	M	6	3/4	4	3	X	X	X	X	X
BCN	1468	ADNC	64	M	10	3/3	1	2	X	0	X	X	X
BCN	1679	ADNC	90	F	12	3/3	1	3	X	X	X	X	X
BCN	1858	ADNC	83	F	8	3/3	0	1	X	-	X	X	X
BCN	1937	ADNC	83	F	8	3/3	1	2	X	X	X	X	X
BCN	1949	ADNC	86	M	8	3/3	1	1	X	-	X	X	X
BCN	1870	ADNC	97	F	7	3/3	2	2	X	X	X	X	X
UCI	29-93	DS	47	F	5	3/3	3	2	X	0	X	-	X
UCI	43-93	DS	48	M	3	3/3	4	4	X	X	X	X	X
UCI	46-94	DS	62	F	3	3/3	4	4	X	X	X	X	X
UCI	23-95	DS	48	F	2	2/2	2	1	X	X	X	X	X
UCI	42-98	DS	55	F	5	-	4	4	X	X	-	-	-
UCI	30-00	DS	61	M	11	3/3	4	4	X	X	X	X	X
UCI	13-02	DS	46	M	6	2/3	4	3	X	X	X	X	X
UCI	23-04	DS	58	M	3	3/4	3	4	X	-	X	X	X
UCI	33-04	DS	50	F	5	3/4	3	4	X	X	X	X	X
UCI	7-05	DS	54	M	5	3/3	4	4	X	X	X	X	X
UCI	22-05	DS	63	F	19	3/3	4	4	X	X	X	X	X
UCI	30-05	DS	57	F	3	3/3	4	4	X	X	X	X	X
UCI	29-06	DS	45	F	3	3/3	4	4	X	X	X	X	X

Bank	ID	Cohort	Age	Sex	PMI (h)	APOE	$X_{A\beta}$	X_{tau}	IHC	PCA	ELISA	HTRF	CB
UCI	35-06	DS	48	F	18	3/3	1	1	X	X	X	X	X
UCI	31-07	DS	52	F	4	2/4	3	3	X	X	X	X	X
UCI	8-08	DS	57	F	5	3/3	3	3	X	X	X	X	X
UCI	31-08	DS	49	M	2	3/3	4	3	X	X	X	X	X
UCI	32-08	DS	42	F	5	3/4	3	2	X	X	X	X	X
UCI	38-08	DS	63	F	3	3/3	4	4	X	X	X	X	X
UCI	42-08	DS	55	M	5	3/3	3	4	X	X	X	X	X
UCI	8-09	DS	70	M	5	3/3	3	3	X	-	X	X	X
UCI	35-09	DS	66	F	3	3/3	3	3	X	X	X	X	X
UCI	31-10	DS	62	F	2	3/3	3	3	X	X	X	X	X
UCI	1-11	DS	45	F	9	3/3	3	3	X	-	X	X	X
UCI	30-11	DS	66	M	4	3/4	2	3	X	X	X	X	X
UCI	33-12	DS	56	M	5	3/3	3	4	X	X	X	X	X
UCI	36-12	DS	56	F	4	3/3	-	-	X	-	X	X	X
UCI	10-13	DS	56	M	4	4/4	4	4	X	X	X	X	X
UCI	21-14	DS	50	M	4	2/3	4	4	X	X	X	X	X
UCI	2-15	DS	43	M	4	3/3	4	3	X	X	X	X	X
UCI	5-15	DS	51	F	3	3/3	2	0	X	-	X	X	X
UCI	27-15	DS	72	M	5	3/3	0	1	X	-	X	X	X
UCI	32-15	DS	49	M	6	3/3	4	4	X	X	X	X	X
UCI	48-15	DS	55	F	5	3/3	-	-	X	-	X	X	X
UCI	4-16	DS	70	M	4	3/3	3	3	X	X	X	X	X
UCI	3-17	DS	57	M	4	3/3	3	4	X	X	X	X	X
UCI	7-17	DS	47	F	7	3/3	4	4	X	X	X	X	X
UCI	31-17	DS	56	F	5	-	3	4	X	-	X	X	X
UCI	33-17	DS	62	F	7	3/3	2	2	X	X	X	X	X
UCI	39-17	DS	58	M	6	3/4	3	4	X	X	X	X	X
UCI	4-02	AD	83	M	3	3/4	3	4	X	X	X	X	X

Bank	ID	Cohort	Age	Sex	PMI (h)	APOE	$X_{A\beta}$	X_{tau}	IHC	PCA	ELISA	HTRF	CB
UCI	12-12	AD	82	F	6	3/4	3	2	x	x	x	x	x
UCI	14-08	AD	86	M	4	3/3	2	2	x	x	x	x	x
UCI	21-06	AD	82	M	5	3/4	1	1	x	x	x	x	x
UCI	37-15	AD	87	F	4	3/4	3	2	x	x	x	x	x
UCI	46-16	ADNC	78	M	3	3/4	2	0	x	x	x	x	x
UCI	10-17	ADNC	66	F	4	3/4	0	2	x	o	x	x	x
UCI	7-03	ADNC	$\geq 90^\dagger$	M	4	3/3	2	1	x	x	x	x	x
UCI	18-08	ADNC	84	F	4	3/3	2	1	x	x	x	x	x
UCI	14-17	ADNC	89	F	6	2/3	0	0	x	o	x	x	x
MTS	163827	DS	59	F	-	-	-	-	x	o	-	-	-
MTS	927140	ADNC	94	F	7	3/3	0	0	x	o	x	-	x
MTS	503571	ADNC	81	F	23	2/3	0	0	x	o	x	x	x
KCL	A184/89	DS	47	F	24	-	-	-	-	-	x	-	x
KCL	A185/89	DS	46	M	72	3/3	4	4	x	x	x	-	-
KCL	A048/78	DS	42	F	-	-	1	1	x	x	-	-	-
KCL	A046/88	DS	19	F	-	-	0	0	x	-	-	-	-
KCL	A300/72	DS	21	M	21	-	0	0	x	o	-	-	-
KCL	A585/80	DS	41	M	48	-	2	1	x	x	-	-	-
KCL	A025/83	DS	38	M	48	-	1	0	x	o	-	-	-
KCL	A027/83	DS	41	M	24	-	1	0	x	x	-	-	-
KCL	A182/90	DS	65	M	9	3/3	4	4	x	x	x	-	x
KCL	A246/91	DS	54	M	9	2/4	4	4	x	x	x	-	-
KCL	A300/95	DS	63	M	120	3/4	3	3	x	x	x	-	-
KCL	A161/09	DS	56	F	29	3/4	4	4	x	o	x	-	x
KCL	A077/16	DS	37	M	48	3/3	1	0	x	x	-	-	x

[†] This case is approximated as 90 years old in our analyses.

Bank	ID	Cohort	Age	Sex	PMI (h)	APOE	X _{Aβ}	X _{tau}	IHC	PCA	ELISA	HTRF	CB
KCL	A372/18	DS	54	F	20	-	4	4	X	0	X	-	-
KCL	A283/98	AD	40	M	97	3/3	0	0	X	0	X	-	X
KCL	A166/04	AD	43	M	28	3/4	4	4	X	X	X	-	-
KCL	A061/03	AD	55	M	18	-	4	4	X	X	X	-	X
KCL	A085/98	AD	55	M	27	-	4	4	-	X	X	-	X
KCL	A067/02	AD	57	M	43	-	4	4	X	X	X	-	X
KCL	A035/03	AD	59	F	36	-	4	4	X	X	X	-	X
KCL	A348/94	AD	59	M	5	3/3	1	0	X	0	X	-	-
KCL	A228/99	AD	59	F	58	-	4	4	X	X	X	-	-
MCR	BBN_2964	DS	62	F	-	-	-	-	X	-	-	-	-
MCR	BBN_2965	DS	60	M	-	-	-	-	X	-	-	-	-
MCR	BBN_2966	DS	13	M	-	-	-	-	X	0	-	-	-
MCR	BBN_2967	DS	62	F	-	-	-	-	X	-	-	-	-
MCR	BBN_2968	DS	53	M	-	-	-	-	X	-	-	-	-
MCR	BBN_2969	DS	64	M	-	-	-	-	X	-	-	-	-
MCR	BBN_2973	DS	37	F	-	-	1	0	X	X	-	-	-
MCR	BBN_2974	DS	58	M	-	-	-	-	X	-	-	-	-
MCR	BBN_2975	DS	65	M	-	-	-	-	X	-	-	-	-
MCR	BBN_2978	DS	57	M	-	-	-	-	X	-	-	-	-
MCR	BBN_2981	DS	50	M	-	-	-	-	X	-	-	-	-
MCR	BBN_2984	DS	64	M	-	-	-	-	X	-	-	-	-
MCR	BBN_2985	DS	71	M	-	-	-	-	X	-	-	-	-
MCR	BBN_2987	DS	58	F	-	-	-	-	X	-	-	-	-
MCR	BBN_2990	DS	60	M	-	-	-	-	X	-	-	-	-
MCR	BBN_2996	AD	60	M	-	3/4	-	-	X	-	-	-	X
MCR	BBN_3011	DS	38	M	-	-	3	4	X	X	-	-	-
MCR	BBN_3012	DS	58	F	-	-	-	-	X	-	-	-	-
MCR	BBN_3020	DS	58	F	-	-	4	4	X	X	-	-	-

Bank	ID	Cohort	Age	Sex	PMI (h)	APOE	X _{AB}	X _{tau}	IHC	PCA	ELISA	HTRF	CB
MCR	BBN_3021	DS	56	M	-	-	4	4	X	X	-	-	-
MCR	BBN_3022	AD	71	F	-	-	4	3	X	X	-	-	-
MCR	BBN_3057	AD	53	F	-	3/3	4	4	X	X	-	-	X
MCR	BBN_3072	AD	44	M	-	-	4	4	X	X	-	-	-
MCR	BBN_3112	DS	9	M	-	-	-	-	X	0	-	-	-
MCR	BBN_3118	DS	61	F	-	-	-	-	X	-	-	-	-
MCR	BBN_3202	AD	50	M	-	2/3	-	-	X	-	-	-	X
MCR	BBN_3223	AD	65	F	-	3/4	-	-	X	-	-	-	X
MCR	BBN_3224	DS	9	F	-	-	-	-	X	-	-	-	-
MCR	BBN_3252	AD	79	F	-	-	-	-	X	0	-	-	-
MCR	BBN_3253	AD	64	M	-	2/3	4	4	X	-	-	-	X
MCR	BBN_3263	AD	56	M	-	-	3	4	X	X	-	-	-
MCR	BBN_3269	AD	66	M	-	-	3	3	X	X	-	-	-
MCR	BBN_3352	DS	61	F	-	-	-	-	X	0	-	-	X
MCR	BBN_3353	DS	58	F	-	2/3	-	-	X	-	-	-	X
MCR	BBN_3354	DS	62	M	-	3/3	-	-	X	-	-	-	X
MCR	BBN_3355	DS	58	M	-	3/4	-	-	X	-	-	-	X
MCR	BBN_3356	DS	53	F	-	3/4	-	-	X	-	-	-	X
MCR	BBN_3358	DS	60	F	-	3/3	-	-	X	-	-	-	X
MCR	BBN_3363	DS	59	M	-	3/3	-	-	X	-	-	-	X
MCR	BBN_3364	DS	61	M	-	3/3	-	-	X	-	-	-	X
MCR	BBN_3365	DS	55	M	-	-	-	-	X	-	-	-	X
MCR	BBN_3380	AD	65	M	-	3/3	3	2	X	-	-	-	X
MCR	BBN_3417	AD	45	M	79	3/3	3	3	X	-	-	-	X
MCR	BBN_3437	DS	58	M	-	-	-	-	X	-	-	-	X
MCR	BBN_3438	DS	56	F	-	3/3	-	-	X	-	-	-	X
MCR	BBN_3439	DS	62	M	-	3/4	-	-	X	-	-	-	X
MCR	BBN_3440	DS	65	F	-	3/3	-	-	X	-	-	-	X

Bank	ID	Cohort	Age	Sex	PMI (h)	APOE	X _{Aβ}	X _{tau}	IHC	PCA	ELISA	HTRF	CB
MCR	BBN_3441	DS	62	F	-	-	-	-	X	-	-	-	-
MCR	BBN_24361	AD	63	F	54	-	4	4	X	-	-	-	-
MCR	BBN_24555	AD	61	F	102	-	3	4	X	-	-	-	X
MCR	BBN005.28400	AD	59	F	87	-	4	4	X	-	-	-	-
MCR	BBN005.32913	AD	66	F	51	-	3	4	X	-	-	-	X
MCR	BBN_14416	ADNC	89	M	48	2/3	1	2	X	X	-	-	X
MCR	BBN_3446	ADNC	92	F	37	-	2	2	X	0	-	-	X
MCR	BBN_14792	ADNC	90	F	78	3/3	1	0	X	0	-	-	X
MCR	BBN_24212	ADNC	82	F	75	-	2	2	X	X	-	-	X
MCR	BBN_24350	ADNC	76	F	98	-	1	1	X	X	-	-	X
MCR	BBN_25922	ADNC	90	F	103	-	1	2	X	X	-	-	X
MCR	BBN005.32526	ADNC	101	F	136	-	1	1	X	X	-	-	X
HVD	AN02218	DS	51	M	16	3/3	-	-	-	-	X	-	X
HVD	S19497	ADNC	93	F	18	3/3	0	-	X	0	X	-	X
OXF	BBN004.34199	AD	103	F	35	2/3	3	4	X	-	X	X	X
OXF	BBN004.26244	AD	75	M	46	3/4	3	4	X	X	X	X	X
OXF	BBN004.26238	AD	87	F	68	3/4	3	4	X	X	X	X	X
OXF	BBN_19683	AD	90	F	48	3/3	3	4	X	X	X	X	X
OXF	BBN004.32861	AD	80	F	78	3/3	3	4	X	X	X	X	X
OXF	BBN004.28928	DS	32	M	96	-	1	2	X	X	-	-	-
OXF	BBN004.28911	DS	7	F	72	-	0	0	X	0	-	-	-
OXF	BBN004.26750	DS	35	M	-	-	1	1	X	0	-	-	-
OXF	BBN004.26748	DS	11	M	10	-	0	0	X	-	-	-	-
OXF	BBN004.26647	DS	13	F	-	-	1	-	X	0	-	-	-
OXF	BBN004.26645	DS	22	M	-	-	-	-	X	-	-	-	-
OXF	BBN004.26644	DS	39	F	95	-	-	-	X	0	-	-	-
OXF	BBN004.26635	DS	36	M	-	-	2	2	X	X	-	-	-
OXF	BBN004.26632	DS	27	F	86	-	0	-	X	0	-	-	-

Bank	ID	Cohort	Age	Sex	PMI (h)	APOE	X _{AB}	X _{tau}	IHC	PCA	ELISA	HTRF	CB
OXF	BBN004.26630	DS	42	F	-	-	1	0	x	x	-	-	-
OXF	BBN004.26628	DS	42	M	72	-	2	1	x	x	-	-	-
NYU	00-059	DS	33	-	-	-	2	2	x	o	-	-	-
NYU	01-035	DS	23	-	-	-	-	-	x	-	-	-	-
NYU	11-233	DS	47	-	-	-	-	-	x	-	-	-	-
NYU	16-245	DS	48	-	-	-	-	-	x	-	-	-	-
NYU	18-052	DS	58	-	-	-	-	-	x	-	-	-	-
UCSF	2509	ADNC	103	M	-	3/3	2	2	x	x	-	-	-

APPENDIX D



University of California
San Francisco

Human Research Protection Program Institutional Review Board (IRB)

Exempt Certification

Principal Investigator

Carlo Condello, PhD

Study Title: Investigation of amyloid conformational diversity and its role in the development of Alzheimer' s disease using fluorescent small-molecule probes

IRB #: 18-25757

Reference #: 226055

Committee of Record: Parnassus Panel

Type of Submission: Submission Correction for Initial Review Submission Packet

Certification Date: 08/15/2018

IRB Comments:

This research qualifies as exempt under the following category:

(4) Research involving the collection or study of existing data, documents, records, pathological specimens, or diagnostic specimens, if these sources are publicly available or if the information is recorded by the investigator in such a manner that subjects cannot be identified, directly or through identifiers linked to the subjects.

Modifications: For exempt research only, researchers can make *minor* changes to the study without notifying UCSF IRB. However, significant changes must be submitted to the UCSF IRB. The UCSF IRB website includes [examples of minor vs. significant changes](#). All changes must follow UCSF guidance, and some changes are not allowed in the [consent materials](#).

Study Closeout Report: This study does not have an expiration date. However, you are required to submit a [study closeout report](#) at the completion of the project.

For a list of [all currently approved documents](#), follow these steps: Go to My Studies and open the study – Click on Informed Consent to obtain a list of approved consent documents and Other Study Documents for a list of other approved documents.

San Francisco Veterans Affairs Medical Center (SFVAMC): If the SFVAMC is engaged in this research, you must secure approval of the VA Research & Development Committee in addition to UCSF IRB approval and follow all applicable VA and other federal requirements. The UCSF IRB [website](#) has more information.

Publishing Agreement

It is the policy of the University to encourage open access and broad distribution of all theses, dissertations, and manuscripts. The Graduate Division will facilitate the distribution of UCSF theses, dissertations, and manuscripts to the UCSF Library for open access and distribution. UCSF will make such theses, dissertations, and manuscripts accessible to the public and will take reasonable steps to preserve these works in perpetuity.

I hereby grant the non-exclusive, perpetual right to The Regents of the University of California to reproduce, publicly display, distribute, preserve, and publish copies of my thesis, dissertation, or manuscript in any form or media, now existing or later derived, including access online for teaching, research, and public service purposes.

DocuSigned by:

3EC27568A39841F... Author Signature

9/1/2021
Date